August 2013

High Power Gain Guided Index Antiguided Fiber Lasers and Amplifiers

Parisa Gandomkar Yarandi
University of Wisconsin-Milwaukee

HIGH POWER GAIN GUIDED INDEX ANTIGUIDED FIBER LASERS AND AMPLIFIERS

by

Parisa Gandomkar Yarandi

A Dissertation Submitted in

Partial Fulfillment of the

Requirement of the Degree of

Doctor of Philosophy

in Engineering

at

The University of Wisconsin-Milwaukee

August 2013

ABSTRACT

HIGH POWER GAIN GUIDED INDEX ANTIGUIDED FIBER LASERS AND AMPLIFIERS

by

Parisa Gandomkar Yarandi

The University of Wisconsin Milwaukee, 2013
Under the Supervision of Dr. Arash Mafi

Increasing the core size of high-power fiber lasers and amplifiers is highly desired in order to mitigate the unwanted nonlinear optical effects and raise the optical damage threshold. If the core size of conventional index-guided (IG) optical fibers increases, the fiber will become multimode, because it is very difficult to control and fine-tune the index step between the core and cladding to satisfy the single mode condition. Siegman proposed Gain-guided index-antiguided (GG-IAG) fibers as a possible platform for ultra-large-core single-mode operation for lasers and amplifiers.

In this thesis, the beam-quality factor M^2 for the fundamental LP_{01} mode of a step-index fiber with finite and infinite cladding diameter is calculated in the presence of gain as a function of the complex generalized V number. The numerical results agree with analytical work that obtained in our group. It is shown that the M^2 value of a single-mode

gain-guided fiber laser can be arbitrarily large. The results are important for the interpretation of the beam-quality measurements in recent experiments on single-mode gain-guided fiber lasers. It is also shown that the conventional infinite cladding diameter approximation cannot be used for index-antiguided gain-guided fibers, and the rigorous analysis is required for accurate prediction of the beam quality factor, as reported in recent experimental measurements.

We also highlight the key reasons behind the poor power efficiency observed in multiple experiments in gain guided index-antiguided (GG-IAG) fiber amplifiers and lasers. We show that by properly designing the fiber geometrical characteristics, it is possible to considerably improve the power efficiency of GG-IAG fiber amplifiers in end-pumping schemes.

This thesis is dedicated to my wonderful parents

For their endless love, support and encouragement

and

to the love of my life!

~ My Husband, Amin ~

For his love and affection, support, patient and friendship

TABLE OF CONTENTS

LIST OF FIGURES

Chapter 1

Chapter 2

Chapter 3

Chapter 4

LIST OF TABLES

Chapter 1

Chapter 4

ACKNOWLEDGEMENTS

I would like to express my gratitude towards many individuals whose help and assistance, made this dissertation possible to carry out. Firstly, I would like to acknowledge Prof. Arash Mafi. Without his continuous support, mentorship, patience, and invaluable inspiration, I would not have been able to develop the comprehension and understanding of my research. I also would like to thank my defense committee Prof. George Hanson, Prof. Chiu-Tai Law, Prof. Vishnuteja Nanduri and Prof. Hossein Hosseini for providing their time and valuable suggestion. Additionally, I want to express my gratitude towards the Department of Electrical Engineering at University of Wisconsin–Milwaukee for giving me the opportunity to pursue my Doctoral studies and contributing the financial support essentially for my research. I wish to acknowledge Dr. Krishna Mohan Gundu in our group. He carried out the analytical derivations for beam quality factor. We compared and confirmed our numerical calculation with his analytical results. I would like to acknowledge Prof. A. E. Siegman, Prof. Michael Bass, Prof. Martin C. Richardson, Prof. John Ballato, Dr. William Hageman, Prof. Bo Peng and Prof. Tsing-Hua Her and their group, whom my research was inspired by their analytical, numerical and experimental research on gain guided, index and antiguided fiber. I had a better understanding when I studied their publications. I want to thank my lab colleagues, Salman Karbasi, Dr. Elham Nazemosadat, Hamed Pourbeyram, Seyed Rasoul Hosseini, Craig Mirr, Aaron D Mueller and Ryan Frazier for their friendship, help and support. I want to thank all my friends in Milwaukee for their continuous help and emotional support throughout my study.

I would like to thank my parents and my brother. They were always supporting me and encouraging me with their best wishes. Finally, I would like to thank my husband, Amin Hassanzadeh. He was always there cheering me up and stood by me through the good times and bad.

Chapter 1

Introduction

1.1 Introduction

A regular fiber consists of two parts; core and cladding, Fig. (1-1). In a regular fiber, the refractive index of the core is higher than the refractive index of cladding, thus, light propagates through the fiber based on the total internal reflection phenomenon. Fig. (1-2) shows the distribution of refractive index in the core and cladding in a step index fiber.

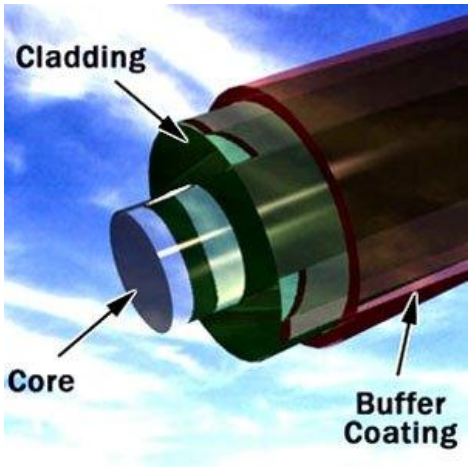

Fig. (1-1). A regular fiber [1].

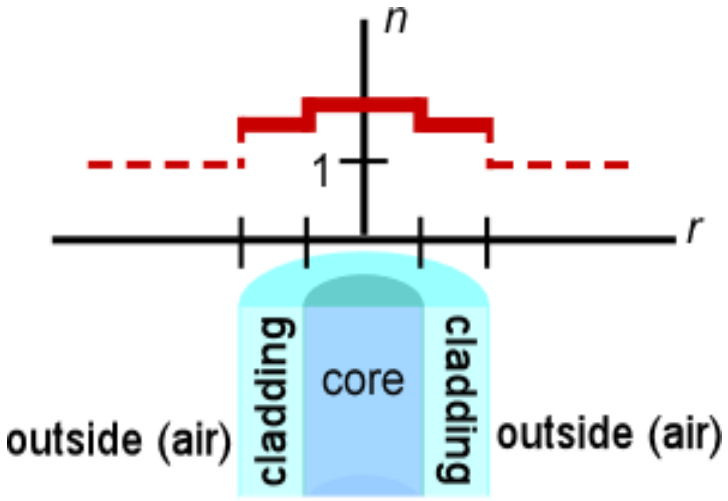

Fig. (1-2). Distribution of refractive index in the core and cladding of a step index fiber [2].

In an optical fiber, the normalized frequency, V (also called the V number), is given by

$$V = \frac{2\pi a}{\lambda}\sqrt{n_1^2 - n_2^2} \tag{1-1}$$

where a is the core radius, λ is the wavelength in vacuum, n_1 is the refractive index of the core, and n_2 is the refractive index of the cladding. The V number determines the number of supported modes in a regular fiber. In a conventional step index fiber the V parameter is equal or less than 2.405, and the fiber supports only one mode per polarization direction. Multimode fibers have higher V numbers.

Optical fibers are classified in different ways. When categorizing optical fiber based on the distribution of the refractive index inside the core, they fall into two groups: 1) Graded Index Fiber (GIF) and 2) Step Index Fiber (SIF). In the SIF category, the refractive index of the core is constant while it decreases gradually in the GIF category, i.e., from its maximum value n_1 at the core center to n_2 at the core cladding interface. Fig. (1-3) (left and middle) shows the schematics of the distribution of refractive index in GIF and SIF, respectively.

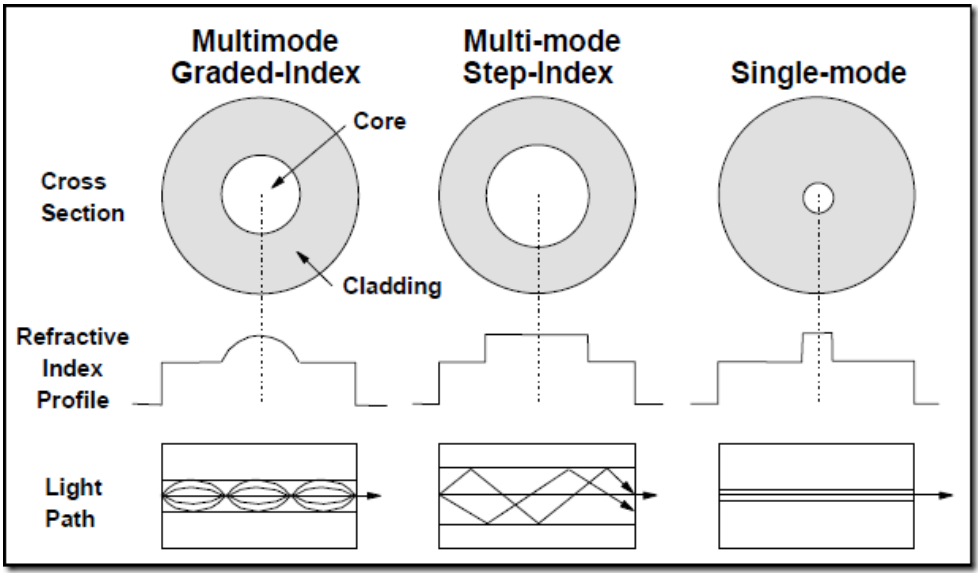

Fig. (1-3). Distribution of refractive index in Multimode Graded-Index Fiber (left), Multimode Step-Index Fiber (middle), and Single Mode Fiber (right) [3].

Optical fibers can be also categorized based on the value of the V parameter to: 1) Single Mode Fiber (SMF) and 2) Multimode Fiber (MMF). Single Mode Fibers only support the fundamental mode and have a small glass core. SMFs are used for high speed data transmission over long distances, and are less susceptible to attenuation and have much higher bandwidth than MMFs. The V parameter in these fibers is less than 2.405. MMFs usually have larger cores than SMFs. Fig. (1-3) (middle and right) shows the different core size of MMFs and SMFs. In Fig. (1-4), the electric field profiles of SMF and MMF are depicted. It is shown that the profile of the output field in SMF has a Gaussian shape while the combinations of the different modes make a non-gaussian shape field in MMF. Note that Fig. (1-4b) shows the combination of the first five modes as the output profile of MMF.

Single mode fibers and Multimode fibers can both be used as fiber lasers. Single mode fiber lasers are typically made with fibers with a core diameters around $9\mu m$. They can produce a narrow, high quality beam.

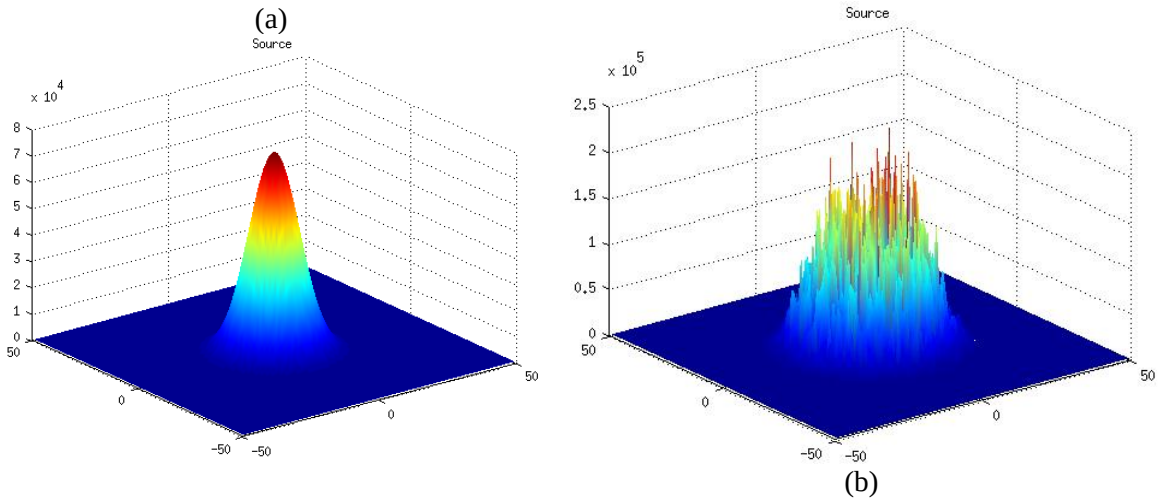

Fig. (1-4). Output electric field profile of, a) SMF and b) MMF.

The high intensity, produced by the small spot in SMF-lasers is ideally suited for laser cutting applications. Multimode fiber lasers, in contrast, utilize fibers with core diameters

between 50–300 μm. Hence, larger core diameter results in lower intensity, more uniform, and flat top beams than small core diameter. In laser science, it is usually desired to use single mode fibers because light can be focused down to a small spot size.

Beam quality factor, M^2, is a parameter that shows whether the output profile has a Gaussian shape (the output of a SMF) or not. M^2 is defined as the ratio of the beam parameter product (BPP) of an actual beam to that of an ideal Gaussian beam at the same wavelength. The beam parameter product of a laser beam is defined as the product of the beam radius that is measured at the beam waist and the beam divergence half-angle. Note that the divergence half-angle is measured in the far field. Thus, if the value of M^2 is near unity, it means that the output profile looks like a Gaussian or single mode and if the value is much greater than unity it implies that the output profile is highly non-Gaussian or multimode. In the next chapters, we will study the beam quality factor and the method for its calculation in detail.

High power fiber lasers and amplifiers have many applications in commercial and military. The two principle limitations to improve the amount of power at the output of high power fiber lasers in conventional SMFs are: 1) the nonlinear optical effects (stimulated Brillouin and Raman scattering) and 2) destructive optical damage in the core and at the fiber end facets. These limitations can be avoided with developing single mode fiber lasers with large mode areas (LMA) fibers. LMA fiber is a fiber in which its core size is increased without compromising the near diffraction limited beam quality of the fiber. A large core diameter, i.e., up to 40 μm, has already been demonstrated with conventional step-index LMA fibers [4]. Single mode laser operation has also been achieved with photonic crystal fibers with core diameter up to 100 μm [5-6]. However,

beyond this core diameter, near diffraction limited beam quality is difficult to maintain. There are other approaches being pursued to investigate the possibility of further increase in the size of core and yet maintaining the single-mode characteristic. An approach pioneered at OFS Laboratories proposes to design a fiber that supports many modes but operates in single mode, specifically chosen Higher Order Mode (HOM) [7]. Such HOM fibers allow expressive increase in effective area up to 4000μm^2. If we compare HOM with conventional Large Mode Area (LMA) fiber with 900 μm^2, HOM fibers enable more amplification with low levels of nonlinearity. HOM fibers with ultra large area can be fabricated that are amenable to simple fusion splicing to standard single mode fiber.

Another approach in designing LMA is chirally coupled core (CCC). The CCC is a technology in which the primary core of the fiber is surrounded by a smaller, lossy core. The smaller core wraps around the primary gain core in a helical pattern along the length of the fiber. The purpose of the secondary chiral core is to provide a loss mechanism for higher order modes that extends into the surrounding cladding from the central core [8-9]. These fibers have the advantage of not requiring a low numerical aperture main core for creating very high quality single mode operation. However, the creation of the required perform and fabrication are very difficult. Fig. (1-5) shows the diagram of the chiarally coupled core fiber.

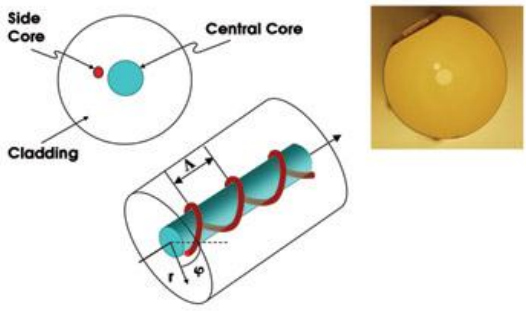

Fig. (1-5). Chirally coupled core structure [10].

Bend-loss management or tapered fiber sections can also be used to filter out higher-order modes. Koplow et al. [11] showed that the bend-loss technique becomes less effective for larger-core fibers. Higher order mode suppression in a 100-μm core fiber is at least a factor of 10 lower than that observed in more commonly used 25 – 50 μm core fibers. The use of tapers for getting high power at the output is also possible, but these not only filter out HOMs, but also limit the output power [12].

The approaches we discussed in previous paragraphs do not involve core sizes larger than 100 μm. Siegman in 2003 proposed a new type of fiber, Gain Guided, Index AntiGuided (GG-IAG) fiber that can have an ultra large core size and also simultaneously operate as single mode [13]. He suggested that if a material with lower refractive index is used for the core, in comparison with cladding, the core size can be increased up to 400 μm in diameter and the fiber can still operate as single mode. However, the total internal reflection mechanism which is responsible for light guiding in conventional optical fiber does not hold if the core refractive index is lower than the cladding; thus the wave cannot propagate through the fiber in normal circumstances. In order to solve this problem and obtain a guiding mode, an amount of gain must be added to the core to constantly amplify the part of the wave that remains in the core as the wave propagates along the fiber. Fig. (1-6) shows the distribution of refractive index in GG-IAG fiber.

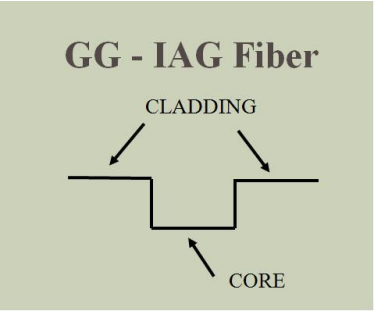

Fig. (1-6). Refractive index distribution in a GG-IAG fiber.

Gain which is added to the core can be considered as an imaginary part of refractive index; therefore, the V parameter becomes a complex number.

$$V^2 = \left(\frac{2\pi a}{\lambda}\right)^2 ({n_1}^2 - {n_2}^2) = \Delta N + i\Delta G, \tag{1-2}$$

We can substitute n_1 (core refractive index) and n_2 (cladding refractive index) with $n_1 = (n_0 + \Delta n) + i\frac{g\lambda}{4\pi}$ and $n_2 = n_0$, respectively, where n_0 is the refractive index of the cladding, Δn is the index step of the fiber core relative to cladding, g is the power-gain coefficient, and λ is the vacuum wavelength.

$$V^2 = \left(\frac{2\pi a}{\lambda}\right)^2 \left((n_0 + \Delta n + i\frac{g\lambda}{4\pi})^2 - {n_0}^2\right) \tag{1-3}$$

$$V^2 = \Delta N + iG \approx \left(\frac{2\pi a}{\lambda}\right)^2 \left(2\mathrm{n}_0\Delta n + \mathrm{i}2n_0(\frac{g\lambda}{4\pi})\right) \tag{1-4}$$

$$\Delta N = \left(\frac{2\pi a}{\lambda}\right)^2 (2\mathrm{n}_0\Delta n) \tag{1-5}$$

$$G = \left(\frac{2\pi a}{\lambda}\right)^2 (\frac{n_0\lambda}{2\pi})\mathrm{g} \tag{1-6}$$

In Eq. (1-4) we assume that Δn and g are very small numbers. If Δn is a positive number, the fiber is Index Guided (IG), and if Δn is a negative number, the fiber is Index AntiGuided (IAG). Siegman studied the modal behavior of a GG fiber over the 2D complex V^2 plane [14]. The horizontal axis is ΔN, real part of V^2, and the vertical axis is G, the imaginary part of V^2, Fig. (1-7). Specifically, Siegman solved the dispersion equation for the first two modes and derived an analytical formula for the threshold line of LP_{01} and LP_{11} in a plane of $(\Delta N, G)$. His proposed formulae for the thresholds of LP_{01} and LP_{11} for $|\Delta N|$ less than 50 is given by [14].

$$G_{th} \cong \sqrt{\frac{4j_{01}^4}{-\Delta N}} = \sqrt{\frac{133.8}{-\Delta N}}\,, [LP_{01}\ mode] \tag{1-7}$$

$$G_{th} \cong \sqrt{\frac{4j_{11}^4}{-\Delta N}} = \sqrt{\frac{862.2}{-\Delta N}}, [LP_{11}\ mode] \tag{1-8}$$

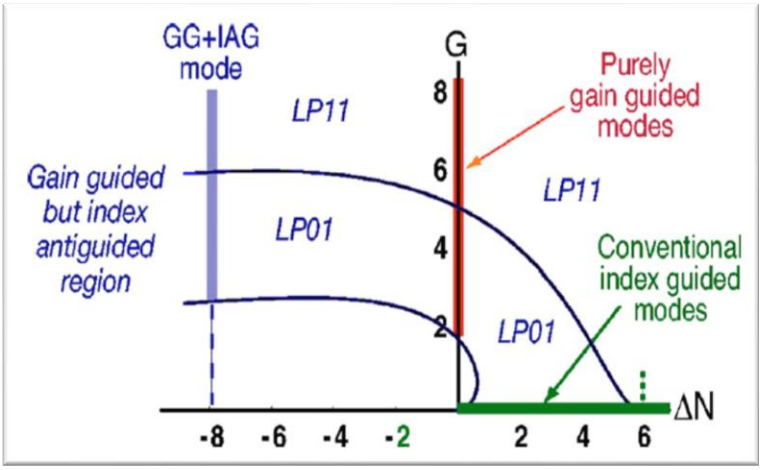

Fig. (1-7). Complex V^2 plane. The horizontal axis , ΔN, is the real part of V^2, and the vertical axis, G, is the imaginary part of V^2, [14].

Based on Fig. (1-7), Siegman mentioned that different combinations of (ΔN and G) can be chosen. The combination of ΔN and G can be any points under the LP_{01} boundary, between two boundaries of LP_{01} and LP_{11}, and above the LP_{11} line. Based on the position in the graph, they are defined as the leaky mode region, single mode region, and multi-mode region, respectively. The electric field under the LP_{01} boundary, between two boundaries of LP_{01} and LP_{11}, and above the LP_{11} line looks like a leaky mode, single mode and multimode, consequently. We can find the distribution of electric field through the core and cladding by solving the Helmholtz equation for LP_{01} and $LP_{11}$with boundary condition at the core cladding interface as Eq. (1-9) and (1-10) [14]:

$$\tilde{E}_{01}(r) = \begin{cases} J_0\left(\frac{\tilde{u}r}{a}\right), & r < a \\ \left[\frac{J_0(\tilde{u})}{K_0(\tilde{w})}\right] K_0\left(\frac{\tilde{w}r}{a}\right), & r > a \end{cases} \tag{1-9}$$

$$\tilde{E}_{11}(r) = \begin{cases} J_1\left(\frac{\tilde{u}r}{a}\right), & r < a \\ \left[\frac{J_1(\tilde{u})}{K_1(\tilde{w})}\right] K_1\left(\frac{\tilde{w}r}{a}\right), & r > a \end{cases} \tag{1-10}$$

Electric field and its slope should be continuous at the core cladding interface. By applying this condition we can find dispersion equation for the first two modes as follows:

$$\frac{\tilde{u}J_1(\tilde{u})}{J_0(\tilde{u})} = \frac{\tilde{w}K_1(\tilde{w})}{K_0(\tilde{w})} \qquad (LP_{01}mode) \tag{1-11}$$

$$\frac{\tilde{u}J_0(\tilde{u})}{J_1(\tilde{u})} = -\frac{\tilde{w}K_0(\tilde{w})}{K_1(\tilde{w})} \qquad (LP_{11}mode) \tag{1-12}$$

In Fig. (1-8) the profile of the electric field for a fixed ΔN and three different values of G (below, on, and above LP_{01} line) are shown. It is depicted that when the value of G is below the threshold, the electric field looks like a leaky mode.

In the next section, we will review all of the theoretical and experimental state-of-the-art researches on this type of fiber.

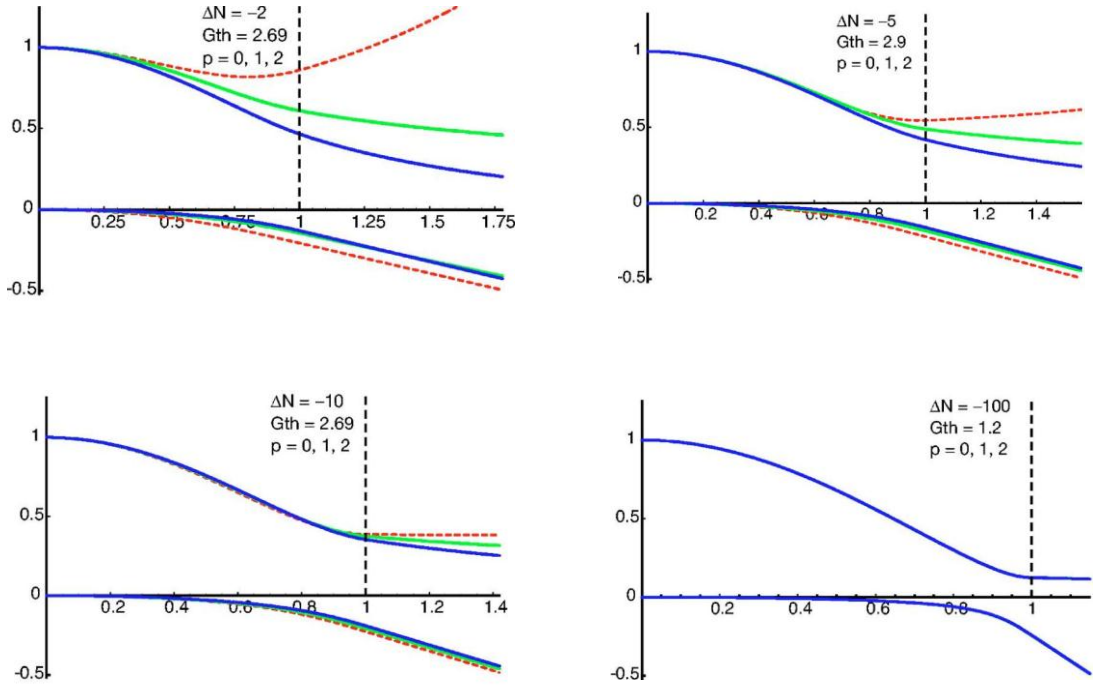

Fig. (1-8). Field amplitude and phase profiles (vertical axis) for the propagating modes in GG-IAG optical fibers for different ΔN = -2, -5, -10, and -100versus the normalized radial distance ($\frac{r}{a}$). Each plot shows the mode profiles for three values of the dimensionless gain parameter, namely G=0 (dashed curves), $G = Gth$ (light curves), and $G = 2Gth$ (dark curves), [14].

1.2 Previous published research

Three years after proposing the idea of GG-IAG fiber by Siegman [13], the first experiment was conducted by a group in the Center for Research and Education in Optics and Lasers (CREOL) in Florida [15]. Siegman et al. used a 10% Nd doped GG-IAG fiber laser with the refractive index of core and cladding equal to 1.5689 and 1.5734, respectively [15]. The core diameter of the fiber was 100 μm and it was $12-15$ cm long. Fig. (1-9) shows the cross section of this fiber. They used a flash lamp for pumping the fiber. A diffuse flash lamp pump cavity was modified to hold 12–15 cm length of this fiber inside a capillary tube with a contacted 100% mirror at one end of the fiber and a polished but uncoated face at the output. The setup is shown in Fig. (1-10).

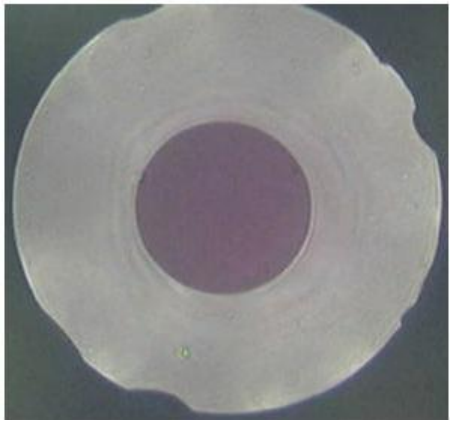

Fig. (1-9). Nd: phosphate GG-IAG fiber [15].

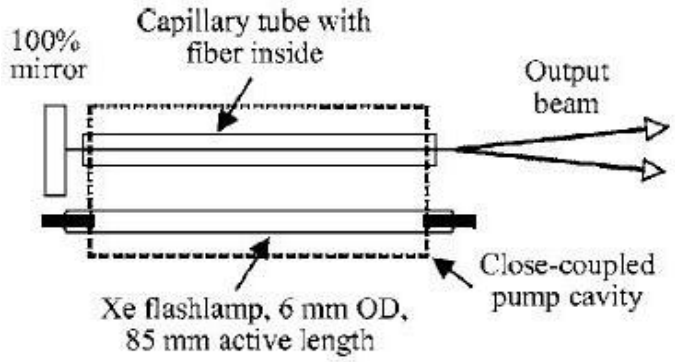

Fig. (1-10). Flash lamp pump cavity used for experimental test [15].

This arrangement means that a centimeter or two of the fiber was left unpumped or only partially pumped in the last segment where the capillary and fiber are extended through the end walls of the pump cavity. Siegman et al. increased the pump energy gradually and measured the output signal energy. The reported value is shown in Fig. (1-11). As depicted in Fig. (1-11), the pump lasing threshold is 50J and it can be improved to 33J with improved fibers. Observation of the output spectrum from the fiber showed that above the threshold, the spectrum is located at the center of the 1052 nm gain line of Nd ions and is a single peak to within the resolution limit of the spectrometer. In Fig. (1-12) the far field intensity profile shows a stable single mode profile. Although the profile of the field is single mode, the value of beam quality factor is not unity ($M^2 \leq 2$).

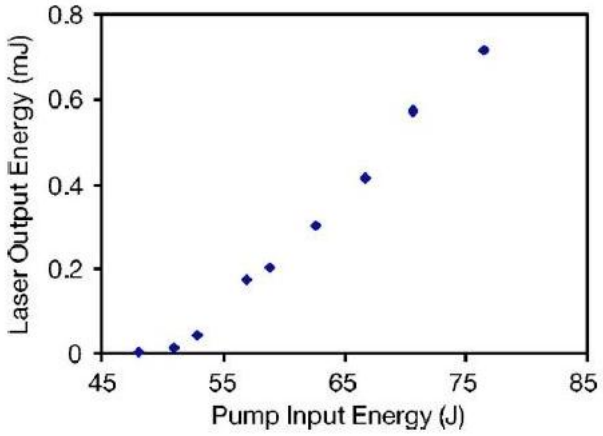

Fig. (1-11). Laser output energy vs. input energy for one of the fiber samples [15].

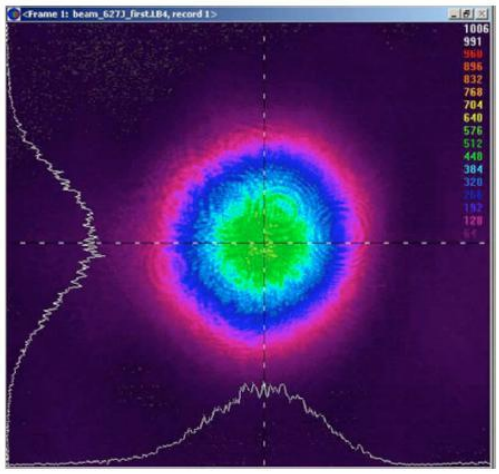

Fig. (1-12). Far field intensity profile for the output beam [15].

As another experiment on the performance of GG-IAG fiber, Chen et al. pumped different GG-IAG fibers with flash lamps [16]. They used a Xe-filled flash lamp having an 8.5 cm long discharge. It produced pulses of $\sim 350\ \mu s$ duration at 1 Hz to pump a GG-IAG fiber of $\sim 13\ cm$ long fibers.

Similar to the aforementioned experiment performed by [15], the output power was low, but results were single mode output profile as depicted in Fig. (1-13). All of the images in Fig. (1-13) were obtained with the CCD camera located at 113 mm from the output coupler. When fitted to a gaussian distribution, the full width at $1/e^2$ of the intensity patterns $(2w_0)$ in Figs. (1-13b)-(1-13d) are, respectively, 1.26, 0.81, and 0.55 mm, each with an experimental error of $\pm 5\%$. When the core diameter becomes large the spot sizes becomes small.

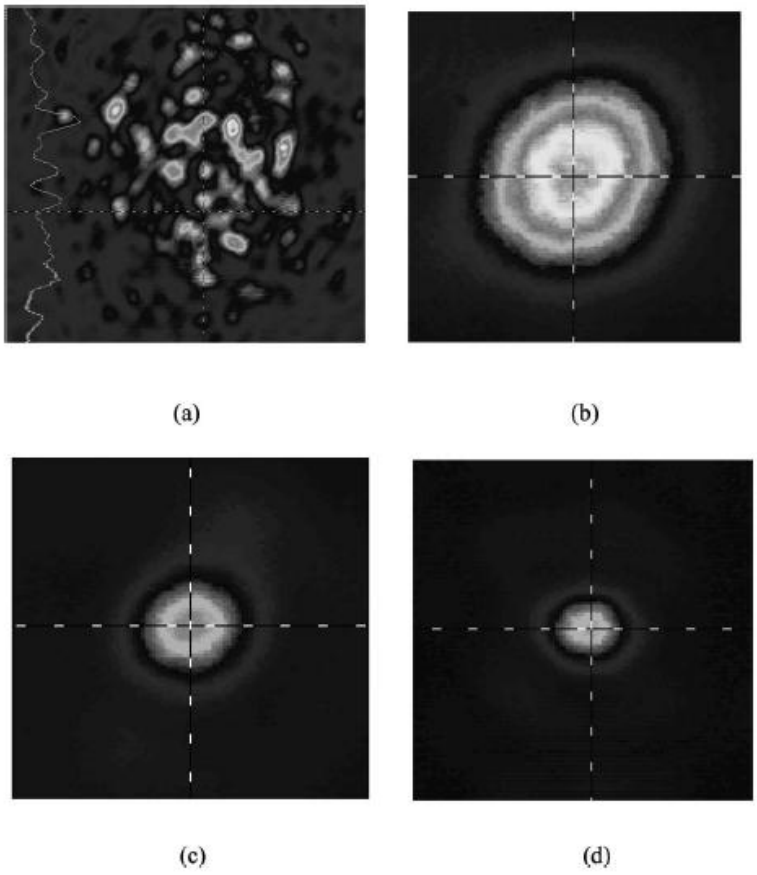

Fig. (1-13). (a) Output pattern due to parasitic modes when no GG-IAG lasing takes place. (b) Single lowest-order mode pattern from the 200 μm core diameter fiber at $6X$ threshold. (c) Single lowest-order mode pattern from the 300 μm core diameter fiber at $7X$ threshold. (d) Single lowest-order mode pattern from the 400 μm core diameter fiber at $10X$ threshold [16].

All measurements results of different GG-IAG fibers are summarized in Table (1-1).

Table (1-1). Measurements results of 100-400 μm core diameter GG-IAG fiber lasers [16]

Fiber core Diameter(μm)	g_{gg}^{01}	g_{gg}^{11}	Range of Reflectivities for lowest order single mode lasing	Output coupler used to achieve single mode	g_{th}^{osc} Calculated for the Mirror used (α) Assumed to be 5%	M^2
100	0.1406	0.3506	4%-10%	4%	0.1988	$1.5\pm$ 10%
200	0.0176	0.0446	65%-75%	75%	0.0178	$1.2\pm$ 10%
300	0.0052	0.0132	88%-91%	90%	0.0065	< 1.8
400	0.0022	0.0056	95%-96%	95%	0.0025	< 1.8

In the two experiments we have reviewed so far [15-16], a flash lamp is used for pumping the fiber. As mentioned by the authors in the conclusions of [15] and [16], the low power of the output was due to the low efficiency of the flash lamp. In another

experiment, in [17], a laser diode with higher efficiency, in comparison with a flash lamp, was used for pumping the fiber. In that experiment, Sudesh et al. used a doped fiber with 1% Nd^{+3} doped $Q100$ phosphate glass in the core. The refractive index of the 100 μm-core radius and 170 μm-cladding radius, measured at 590 nm, was 1.5689 and 1.5734, respectively. The setup of the end pump laser action is demonstrated in Fig. (1-14). The power of the laser diode was 30W, emitted at 803 nm. The power was delivered by the fiber that had 200 μm core diameter and a numerical aperture of 0.22. Free space coupling of the pump light with aspheric lenses produced a 400 μm illumination spot on the end of the fiber. Therefore, less than 0.25% of the pump light was coupled to the core of the IAG fiber.

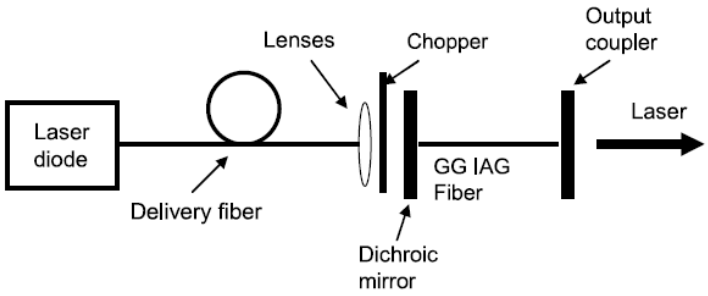

Fig. (1-14). Schematic of the laser diode end pumped a large diameter core GG-IAG fiber laser setup [17].

To reduce the thermal loading on the fiber, the pump light was modulated with a mechanical shutter providing a ~4 ms pump pulse at 14Hz. The output spectrum was measured by an Ocean Optics HR 4000 spectrometer.

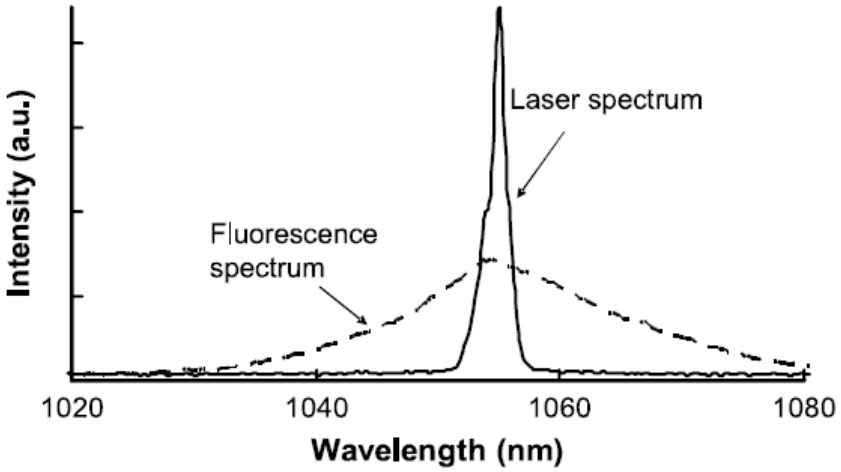

Fig. (1-15). Output Spectral [17].

As depicted in Fig. (1-15), the spectrum is centered at 1055 nm and it narrows down to $\sim 2nm$ width ($FWHM$) when the GG-IAG fiber lases. The measured output power versus input pump power is shown in Fig. (1-16). As depicted, the threshold pump power is around 6W. Furthermore, Fig. (1-17) shows a stable single mode output profile of the field. In this experiment the reported value of M^2 is greater than 1 although the pattern shows a single mode profile.

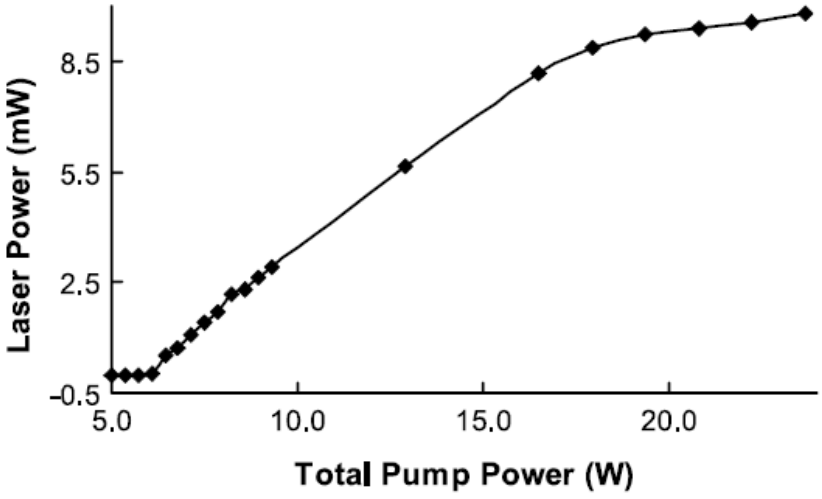

Fig. (1-16). Output power versus total input power [17].

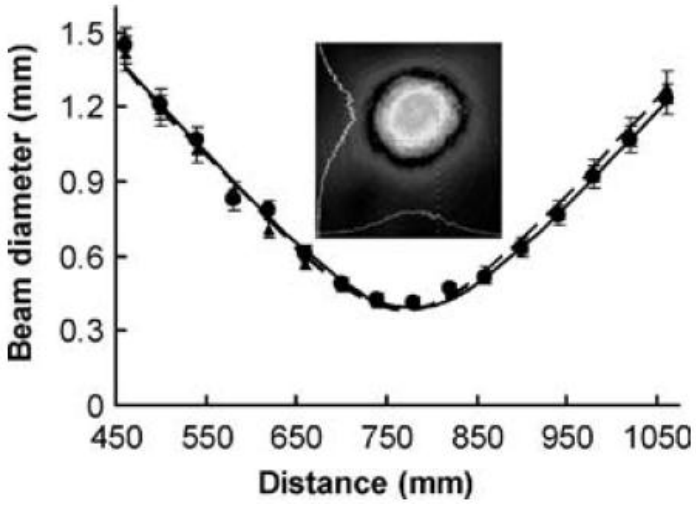

Fig. (1-17). Mode pattern of the laser at the distance of 250 mm from the output coupler [17].

Although in this experiment Sudesh et al. used a higher efficiency pumping method, the results were not improved in comparison with [15] and [16]. The authors mentioned two reasons for that: 1) The nature of IAG in this type of fiber. Because the core has a lower refractive index in comparison with the cladding; therefore, the entire pump wave escapes to the cladding after the first few centimeter of propagation. Thus, the rest of the fiber will not receive any pump power to generate sufficient gain. 2) Thermal problems which are associated with a large diameter fiber laser. When the fiber is pumped, atoms absorbed light energy and will be exited to a higher level. Then they decay rapidly to a lower level. Some of the decay are clearly nonradiative and produce thermal energy. When the core size increases the population of dopant molecules per cross section increases and more thermal load will be produced. The suggested remedies for the thermal problem are: 1) using side pumping methods and 2) using other doping material like Yb, Er or Tm that have a low quantum defect rate.

Siegman, in another paper [14], found an analytical formula for the modal power gain. A modal power gain coefficient g_m can be defined for the guided mode that propagates

along the fiber. It corresponds to the exponential power growth rate for G values above threshold. We can relate g_m to a dimensionless modal gain parameter G_m by

$$G_m \equiv (\frac{2\pi a}{\lambda})^2 \times \left(\frac{n_0 \lambda}{2\pi}\right) \times g_m = 2 w_r w_i \tag{1-13}$$

Eq. (1-13) can be used to say that the modal gain or loss parameter G_m for the guided eigen-mode is given to a good approximation, both below and above threshold, by

$$G_m \cong G - G_{th} \cong (p-1) \times G_{th} \tag{1-14}$$

where $p = \frac{G}{G_{th}}$ is a normalized pumping power relative to the threshold value for gain guided propagation. Eq. (1-14) indicates that the threshold gain for each mode is approximately equal to the radiation loss or leakage loss for the same mode in the absence of gain.

An effective filling factor η_{01} for the LP_{01} mode for values above threshold in G greater than G_{th} can be defined as $\eta_{01} \equiv \frac{G_{m,01}}{G} \cong (p-1)/p$. This filling factor starts at $\eta_{01} = 0$ for $G = G_{th,01}$ and tends to $\eta_{01} = 1 - \left(\frac{G_{th,01}}{G_{th,11}}\right) \cong 61\%$ as the gain in the core approaches the threshold value for the LP_{11} mode.

Another interesting result from these formulas is that we can substitute Eqs. (1-5), (1-6) in Eqs. (1-11), (1-12) and find the power gain coefficient g_{gg} for the first two modes as follows:

$$g_{gg}^{01} = \sqrt{\frac{133.8}{2n_0^3(-\Delta n)}} \frac{\lambda^2}{(2\pi)^2 a^3} \tag{1-15}$$

$$g_{gg}^{11} = \sqrt{\frac{862.2}{2n_0^3(-\Delta n)}} \frac{\lambda^2}{(2\pi)^2 a^3} \tag{1-16}$$

Based on Eqs. (1-15), (1-16), the modal gain thresholds are proportional to a^{-3}. As the core radius increases, the gain thresholds will decrease. However, if we attempt to keep

the fiber single mode by ensuring a modal gain between g_{gg}^{01} and g_{gg}^{11}, then the modal gain will also be affected by the inverse relationship between the gain and core radius. Thus, using large core GG-IAG fiber does not help to obtain more power at the output.

Another interesting work on GG-IAG fiber is research conducted by a group at the University of North Carolina at Charlotte [18]. In this research, Her suggested using a Bragg fiber for GG-IAG fiber. To keep pump power in the core, Her theoretically designed a photonic band gap to trap the pump light in the core although it was a band pass at signal wavelength [18]. Fig. (1-18) shows the schematic of brag fiber and also the radial index profile.

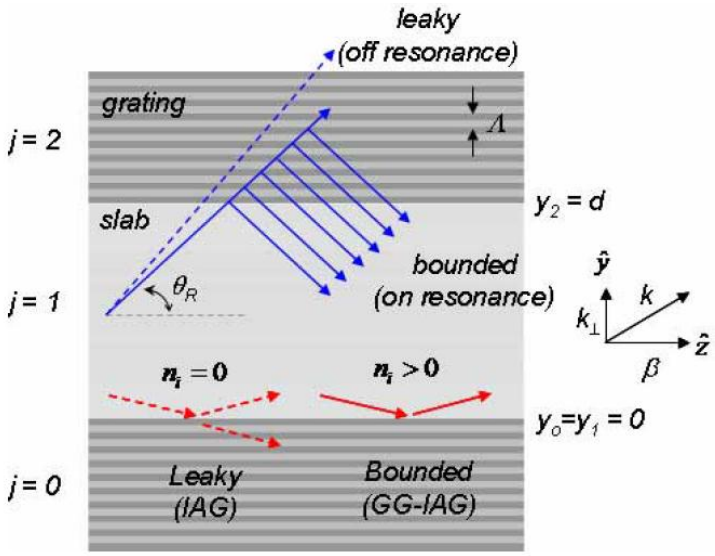

Fig. (1-18). Schematic of a one-dimensional gain-guided transverse grating waveguide. The pump (blue) is confined via Bragg resonance and the signal (red) is confined by gain guiding (GG). Dashed and solid lines indicate leaky and bound rays, respectively [18].

Another research group made a Yb^{+3} doped GG-IAG fiber with core radius of $100\mu m$, inner cladding radius of $200\mu m$, and outer cladding radius of $225\mu m$ [19]. The refractive index of the core and undoped cladding materials measured at 589.3 nm were 1.57224 and 1.57318, respectively. The set up presented in Fig. (1-19) was used for investigating the laser amplifier characteristics of this GG-IAG fiber.

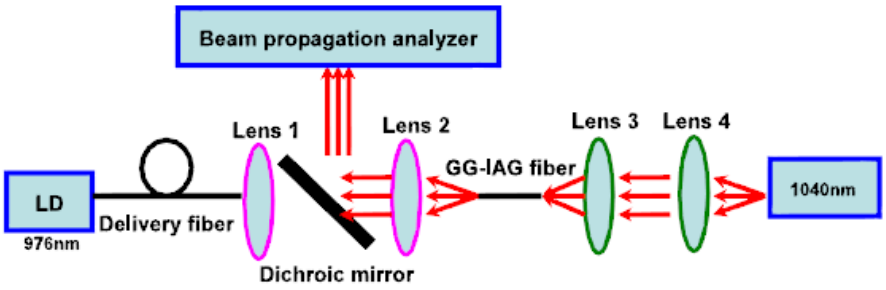

Fig. (1-19). Experimantal setup for laser amplifier and beam quality tests [19].

A $120\,mm$ long GG-IAG fiber acting as a laser amplifier was end pumped by a fiber coupled $\sim 8w$ laser diode which emitted at $976\,nm$. The delivery fiber had a core diameter of 125 μm and a numerical aperture of 0.22. The signal light at 1040 nm was focused by two identical microscope objective lenses, (Lens3 and Lens 4). Then, it was injected with a spot diameter of 160 μm through Lens3 and Lens 4 on the other side of the fiber. The two identical microscope objective lenses worked as couplers. The amplified signal light was collimated by Lens 2 and was reflected to the power detector by a dichroic mirror HR at 1 μm, and HT at 980 nm [19].

The corresponding plot for the output power, as a function of total pump power, is shown in Fig. (1-21). Surprisingly, the output light did not improve, and efficiency of the fiber laser was very low. Lu et al. mentioned that the end face of GG-IAG fiber was not polished well and $\sim 70\%$ of the pump light was lost due to the light scattering. This means that $\sim 30\%$ of the light energy was coupled into the core of the fiber.

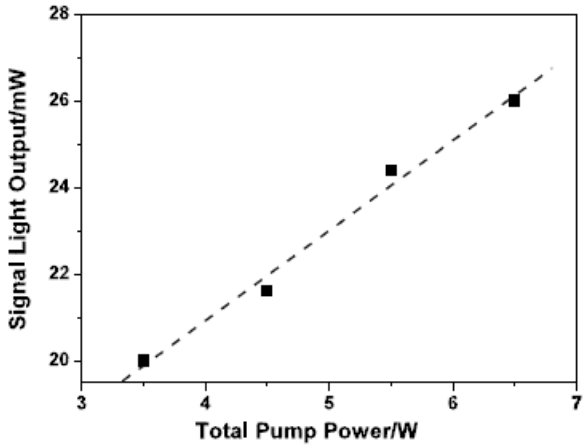

Fig. (1-20). Signal light output versus total pump power [19].

Fig. (1-21) shows the output mode pattern of signal light with maximum pump power ($6.5W$) from experiment in [19]. The beam quality factor of the output of the GG-IAG fiber was also measured in [19]. Although the output profile was like a single mode fiber, the value of M^2 was a large number, i.e., $2 < M^2 < 2.5$. As the conclusion, the authors suggested using a D-shaped and rectangular cladding cross section to improve the pump absorption and substantially increase the optical efficiency of the GG-IAG Yb doped [19].

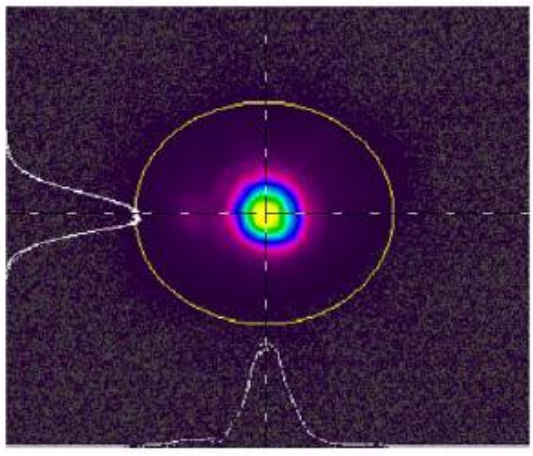

Fig. (1-21). Mode Pattern of signal light [19].

The results of fabrication of a D-shaped fiber in the aforementioned experiment are recently published [20]. The fiber used in that work is depicted in Fig. (1-22). The fiber core radius is 100 μm, the diameter of the D-shaped inner cladding is 315/240 μm for the longer/shorter axis, respectively. The outer cladding is a 380 μm in radius. The refractive indexes of the core and undoped cladding materials measured at 589.3 nm were 1.54221, and 1.52752, respectively.

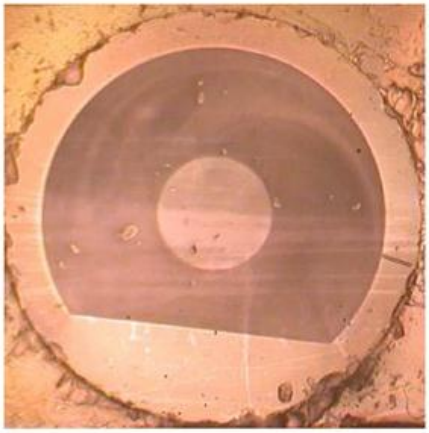

Fig. (1-22). Photograph of the hand-polished end face of Yb^{+3} GGIAG fiber with D-shaped inner cladding [20].

The setup for the investigation of amplifier characteristics in this experiment was like [19], Fig. (1-19). and the result is depicted in Fig. (1-23). Although the symmetry of the previous fiber was broken in the new experiment, the slope efficiency did not improve more than previous experiment reported in [19]. Li et al. concluded that although there was not much improvements in output power, if the symmetry of the cladding changes more, for example by using a Double D (DD) cladding shape or rectangular cladding shape, the pump absorption will be improved [20].

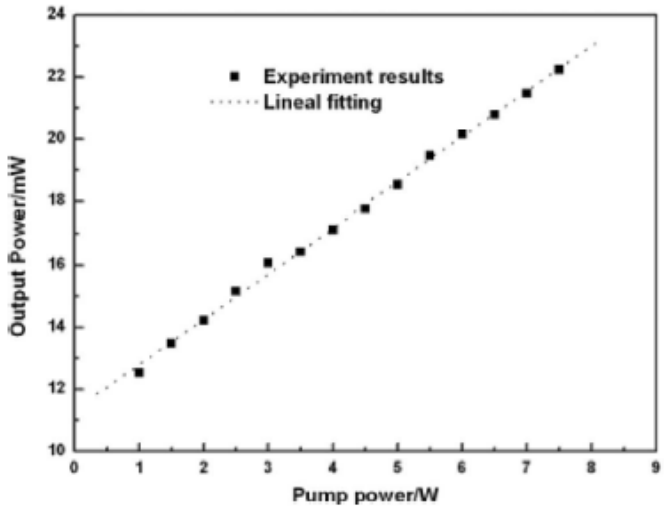

Fig. (1-23). Signal light output verses total pump power [20].

Kim et al. conducted numerical simulation for investigating the thermal issue [21]. They solved the heat equation for fiber by using two boundary conditions for the core-cladding and cladding-environment interfaces. The distribution of heat in core and cladding regions is as follows,

$$T(r) = \frac{Q}{4K_1}(r_1^2 - r^2) - \frac{Q}{2K_2} r_1^2 \ln\left(\frac{r_1}{r_2}\right) + \frac{r_1^2 Q}{2hr_2} + T_F \text{ , } 0 \le r \le r_1 \quad (1\text{-}17)$$

$$T(r) = -\frac{Q}{4K_2} r_1^2 \ln\left(\frac{\mathrm{r}}{\mathrm{r}_2}\right) + \frac{r_1^2 Q}{2hr_2} + T_F, r_1 \le r \le r_2, \quad (1\text{-}18)$$

where Q is the constant heat source density in the core induced by uniform pumping, T_F is the coolant temperature, K_1 and K_2 are the thermal conductivities of the core, and the cladding materials, respectively, and h is the heat transfer function of a coolant [21].

The four graphs in Fig. (1-24), show different situations for temperature distribution in the core center for different parameters.

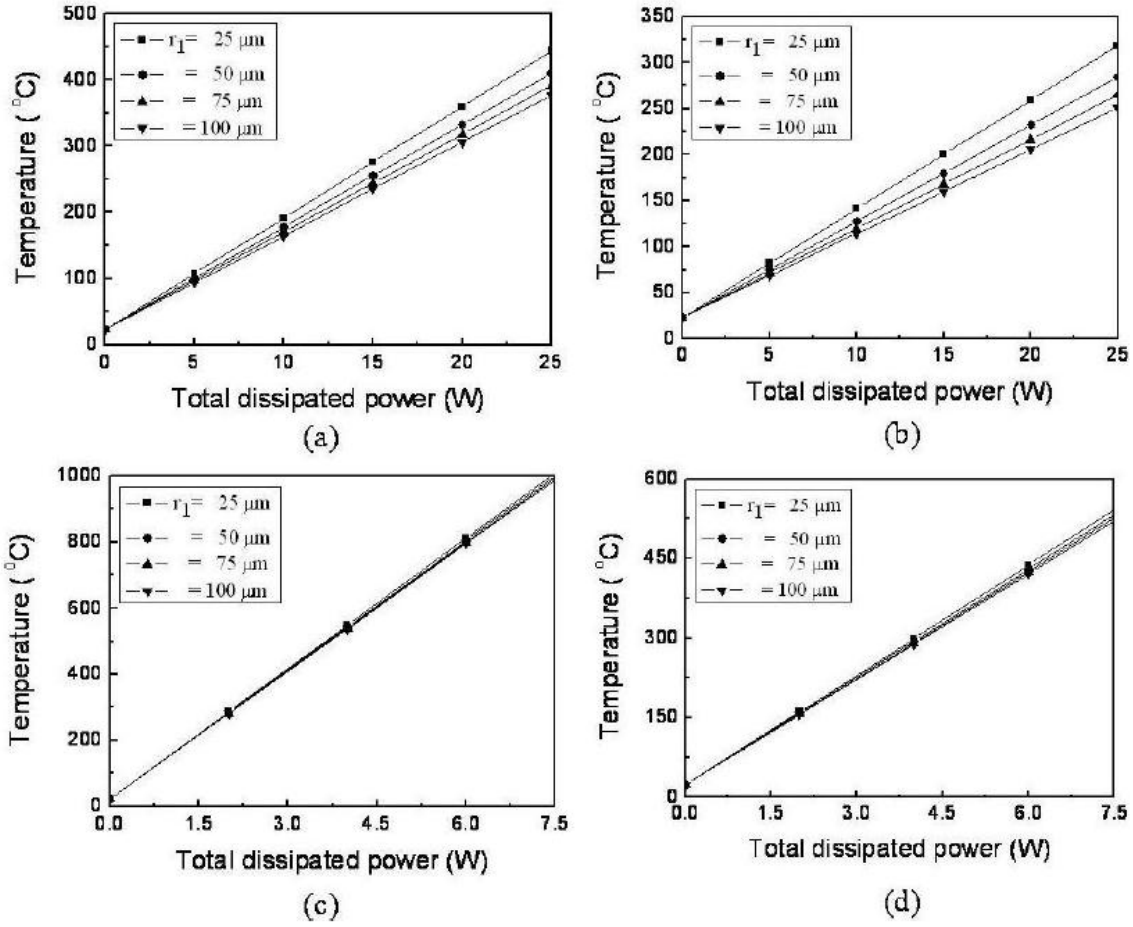

Fig. (1-24). Temperature at the core center of the GG-IAG fiber with a 10-cm length when the total dissipated power increases for the following fiber parameter. (a) $h = 1\ kW/(m^2.K)$, $r_2 = 125\ \mu m$; (b) $h = 1\ kW/(m^2.K)$, $r_2 = 250\ \mu m$; (c) $h = 100\ kW/(m^2.K)$, $r_2 = 125\ \mu m$; (d) $h = 100\ kW/(m^2.K)$, $r_2 = 250\ \mu m$ [21].

The graphs show that with a fixed value for h, the temperature in the core center decreases when the cladding radius increases. The results obtained by the numerical simulations are just opposite to the speculation of the failed attempts by [15-17] as they mentioned that the thermal issue, associated with the large core size, is the main problem in getting high power at the output of GG-IAG fibers. Also, when h parameter increases, the temperature of the core center also increases.

Yan et al. in [22] also made a Yb^{+3} double clad GG-IAG fiber with 100 μm core radius. The difference between the core and cladding refractive index, Δn, was -0.0004. They

performed a numerical simulation based on ray-tracing and studied the absorption characteristics of GG-IAG fiber. They also verified their numerical results with real experiments. Fig. (1-25) shows the setup for the absorption measurement of GG-IAG fiber.

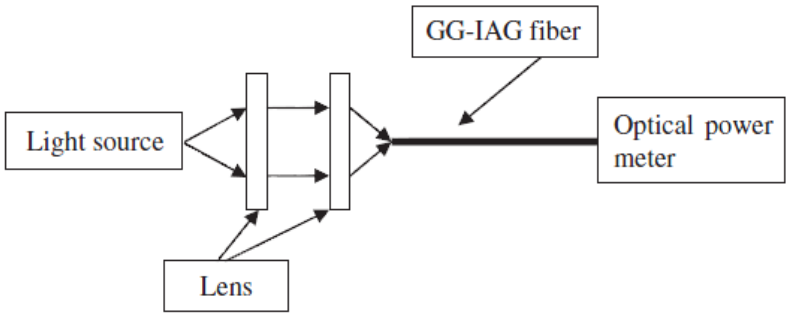

Fig. (1-25). Experimental arrangement for the absorption measurement of the $GG - IAG$ fiber [22].

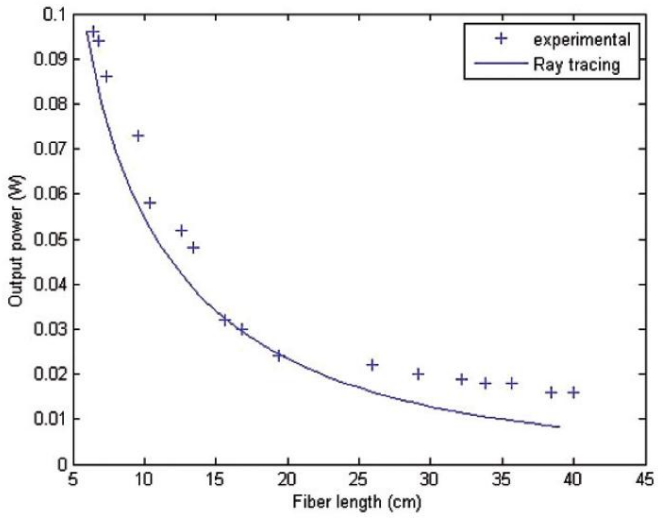

Fig. (1-26). The curves of experiment and simulation for absorption characteristics of the GG-IAG fiber [22].

Fig. (1-26) shows the experiment and simulation results. The interesting point in this graph is that most of the pump power is absorbed in the first few centimeters, thus, there will not be enough pump power for the rest of the fiber. In order to investigate pump absorption, the refractive index difference, Δn, was also changed in that studies. It was observed that as Δn increases, the absorption length increases too [22].

Finally, Hageman et al. in CREOL [23] used side pumping methods for pumping GG-IAG fibers. The fiber was pumped with a Dilas linear array. The beam profile of GG-IAG laser beam is depicted in Fig. (1-27). The measured output versus input energy for a 4 cm long GG-IAG laser is shown in Fig. (1-28).

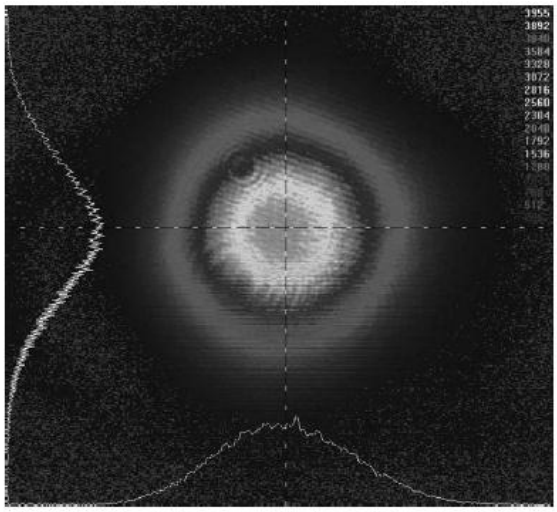

Fig. (1-27). Profile pattern of GG-IAG fiber [23].

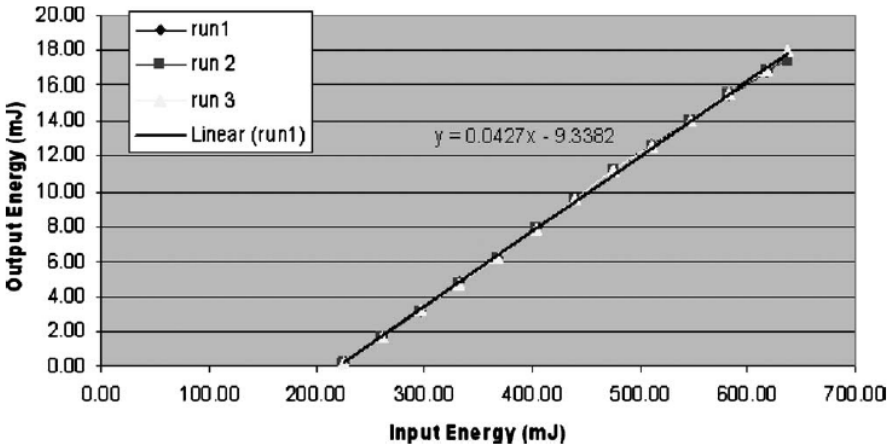

Fig. (1-28). Output energy versus input energy of GG-IAG fiber [23].

Similar to the previous experiments, the results show a stable single mode profile, although the beam quality factor is larger than unity ($M^2 \approx 1.4$) and the slope efficiency of output power is very low (4.3%). In [23], it is suggested that, one can increase the pump efficiency by increasing the core diameter [23]; however, based on the Eqs. (1-15)

and (1-16), $g \propto a^{-3}$, increasing the core radius not only improves the efficiency but also decreases the gain per centimeter.

In this chapter we reviewed recent theoretical and experimental results on GG-IAG fiber. The common results between all the experiments were the large value of Beam quality factor and the low output power. The large beam quality factor was a big, unanswered question because the profile of the field shows a single mode pattern in all the experiments but the measured values of M^2 were in the range of 1.05–2.0. The low output power is another ambiguous issue in GG-IAG fibers that, to the best of our knowledge, has not been satisfactorily addressed. Using a high efficiency method of pumping such as diode laser, changing the doping materials, breaking the symmetry of the fiber and using the brag fiber were not efficient solutions for getting high power at the output. In this thesis we solved the two main problems regarding GG-IAG fibers. In chapter 2 as we will discuss, we calculate the beam quality factor of GG-IAG by considering an infinite cladding. In chapter 3, we modified all of the formulas for the electric field of GG-IAG fibers when the size of the cladding is infinite. Then, we calculated beam quality factor of GG-IAG fibers. Finally in chapter 4, we addressed the second problem related to the low power efficiency of GG-IAG fibers.

1.3 References

[1] http://computer.howstuffworks.com/fiber-optic.htm

[2]http://www.rpi.edu/dept/phys/ScIT/InformationTransfer/reflrefr/rr_content/fibers_20.html

[3] http://www.fiberoptics4sale.com/wordpress/fiber-dispersion-and-optical-dispersion-an-overview/

[4] Y. Jeong, J. Sahu, D. Payne, and J. Nilsson, "Ytterbium-doped large-core fiber laser with 1.36 kW continuous-wave output power," Opt. Express 12, 6088-6092 (2004).

[5] J. Limpert, O. Schmidt, J. Rothhardt, F. Röser, T. Schreiber, A. Tünnermann, S. Ermeneux, P. Yvernault, and F. Salin, "Extended single-mode photonic crystal fiber lasers," Opt. Express 14, 2715-2720 (2006).

[6] C. D. Brooks and F. D. Teodoro, "Multi-megawatt peak-power, single-transverse-mode operation of a 100 μm core diameter, Yb-doped rod-like photonic crystal fiber amplifier," Appl. Phys. Lett. 89(11), 111119 (2006),

[7] S. Ramachandran, J. W. Nicholson, S. Ghalmi, M. F. Yan, P. Wisk, E. Monberg and F. V. Dimarcello, "Light propagation with ultralarge modal areas in optical fibers," Optics Letters, vol. 31, pp. 1797-1799, (2006).

[8] M. C. Swan, C. H. Liu, D. Guertin, N. Jacobsen, K. Tankala, and A. Galvanauskas, "33μm Core Effectively Single-Mode Chirally-Coupled-Core Fiber Laser at 1064-n" Optical Fiber Communication Conference and Exposition and The National Fiber Optic Engineers Conference, (2008).

[9] C. Liu, G. Chang, N. Litchinister, D. Guertin, N. Jacobson, K. Tankala, and A. Galvanauskas, "Chirally Coupled Core Fibers at 1550-nm and 1064-nm for Effectively

Single-Mode Core Size Scaling," in Conference on Lasers and Electro-Optics/Quantum Electronics and Laser Science Conference and Photonic Applications Systems Technologies, (2007).

[10] http://www.photonics.com/Article.aspx?AID=34668

[11] Jeffrey P. Koplow, Dahv A. V. Kliner, and Lew Goldberg, "Single-mode operation of a coiled multimode fiber amplifier," Opt. Lett. 25, 442-444 (2000)

[12] J. D. Minelly, V. Stasyuk, J. P. de Sandro, E. Gagnon, and S. Chatigny, presented at Optical Amplifiers and their Applications (OAA 2004), San Francisco, CA., June 27-30 2004, postdeadline paper PD4-1.

[13] A. E. Siegman, "Propagating modes in gain-guided optical fibers," J. Opt. Soc. Am. A 20, 1617-1628 (2003).

[14] A. E. Siegman, "Gain-guided, index-antiguided fiber lasers," J. Opt. Soc. Am. B 24, 1677 (2007).

[15] A. E. Siegman, Y. Chen, V. Sudesh, M. C. Richardson, M. Bass, P. Foy, W. Hawkins, and J. Ballato, "Confined propagation and near single mode laser oscillation in a gain guided, index antiguided optical fiber," Appl. Phys. Lett. 89, 251101 (2006).

[16] Y. Chen, T. McComb, V. Sudesh, M. C. Richardson, and M. Bass, "Very large-core, single-mode, gainguided, index-antiguided fiber lasers," Opt. Lett. 32, 2505 (2007).

[17] V. Sudesh, T. McComb, Y. Chen, M. Bass, M. Richardson, J. Ballato, and A. E. Siegman, "Diode-pumped 200 m diameter core, gainguided, index-antiguided single mode fiber laser," Appl. Phys. B, vol. 90, pp. 369–372, (2008).

[18] T. H. Her, "Gain-guiding in transverse grating waveguides for large modal area laser amplifiers," Opt. Express, vol. 16, pp. 7197–7202, (2008).

[19] M. Lu, W. Li,K. Zou, S.Dai,W.Wei, and B. Peng, "Yb doped 200 m diameter core, gain-guided index-antiguided fiber," Appl. Phys. B, vol. 98, pp. 301–304, (2010).

[20] W. Li, M. Lu, Z. Yang, H. Guo, P. Wang, and B. Peng, "Fabrication and characterization of Yb doped gain-guided index-antiguided fiber with D-shaped inner cladding," J. Opt. Soc. Amer. B, vol. 28, pp. 1498–1501, (2011).

[21] Hyun Su Kim, V. Sudesh, T. McComb, and Richardson, "Investigation of the thermal characteristics of a Gain-guided Index-anti-guided fiber," J. of the Korean Soc., vol. 56, No. 1, pp. 209–213, (2010).

[22] K. L. Yan, E. Y. Zhou, W. Wei, and B. Peng, "Efficiency of pump absorption in gain-guided and index-antiguided (GG-IAG) fiber," J. Mod. Opt., vol. 57, pp. 480–484, (2010).

[23] W. Hageman, Y. Chen, X.Wang, L. Gao, G. U. Kim, M. Richardson, and M. Bass, "Scalable side-pumped, gain-guided index-anti-guided fiber laser," J. Opt. Soc. Amer. B, vol. 27, pp. 2451–2459, (2010).

Chapter 2

Beam Quality Factor of Single Mode Gain Guided-Index Anti Guided Fiber Lasers With Infinite Cladding Boundary

2.1 Introduction

There has been a growing interest in optical fiber lasers that operate based on the gain guiding-index antiguiding ($GG - IAG$) principle. Unlike a conventional index-guiding (IG) fiber, the core of an index-antiguiding (IAG) fiber has a lower refractive index than the surrounding cladding and cannot support IG modes. Siegman [1] has shown that in the presence of sufficient gain, an IAG fiber can support confined propagating GG modes, which are normalizable in the transverse direction. More interestingly, even for arbitrarily large core diameters, $GG - IAG$ fibers can operate in a robust single transverse mode. It is therefore desirable to take advantage of the $GG - IAG$ principle and scale up the core size while maintaining the single mode characteristic. The large core size is attractive because it can help mitigate unwanted nonlinear optical effects, raise the optical damage threshold, and increase the amplification per unit length of the fiber.

Several experiments have demonstrated $GG - IAG$ in various fiber laser configurations [2–5]. The reported values of the beam-quality factor, M^2, in these experiments are notably larger than unity, even in fibers that are designed to operate as single mode. This should not be surprising considering the substantial departure of the LP_{01} profile of a $GG - IAG$ fiber from a Gaussian-like beam [6], as similarly reported in other unconventional optical fibers [7]. However, we show that the values of M^2 for the single-mode $GG - IAG$ fibers are substantially larger than those measured in the experiments. Therefore, the not-so-puzzling larger than unity M^2 measurements in these fibers turn out to be quite a bit lower than those expected from a pure $GG - IAG$ structure.

A closed-form expression for the M^2 parameter of the LP_{01} mode in the presence of gain as a function of the complex generalized fiber V number is presented in this chapter. The

M^2 parameter has been calculated analytically for the LP_{mn} modes in passive fibers [8]. However, we are not aware of a derivation in the presence of gain, which requires integrals of complex variables and is mathematically more involved.

To study step-index optical fibers in the presence of gain ($GG-IG$ or $GG-IAG$), it is convenient to use a generalized complex $\tilde{V}$ parameter squared [1]; defined as

$$\tilde{V}^2 = \Delta N + i\Delta G, \tag{2-1}$$

The index and gain parameters ΔN and G are given by

$$\Delta N = \left(\frac{2\pi a}{\lambda}\right)^2 (2\mathrm{n}_0\Delta n), \tag{2-2}$$

$$G = \left(\frac{2\pi a}{\lambda}\right)^2 (\frac{n_0\lambda}{2\pi})\mathrm{g}\,, \tag{2-3}$$

where n_0 is the refractive index of the cladding, $n_0+\Delta n$ is the refractive index of the core, a is the core radius, g is the core power-gain coefficient, and λ is the vacuum wavelength. For a proper choice of ΔN and G, the core can support an LP_{01} guided mode in the form of

$$E(x,y,z_0) = \begin{cases} \tilde{N}J_0(ur/a)/J_0(u), \\ \tilde{N}K_0(wr/a)/K_0(u), \end{cases} \tag{2-4}$$

The parameters u and w are complex and satisfy the following two equations, which can be used to determine these parameters, given $\tilde{V}$:

$$\frac{uJ_1(u)}{J_0(u)} = \frac{wK_1(w)}{K_0(w)}, \tag{2-5}$$

$$u^2 + w^2 = \tilde{V}^2. \tag{2-6}$$

$\tilde{N}$ is an overall constant to be determined from the normalization condition (2-7) assumed throughout this chapter.

$$\iint dS|E(x,y,z)|^2 = 1, \tag{2-7}$$

where $\iint dS = \iint dxdy$. In general, the value of $\tilde{V}$ determines the total number of confined guided modes in a fiber in the presence of gain, which can be zero or higher. The single-mode operating regions of the $GG - IG$ and $GG - IAG$ structures in the $\Delta N - G$ Cartesian space are presented in detail by Siegman [1, 6] and we explained it in chapter one.

2.2 Beam Quality Factor

The beam-quality factor M^2 is commonly used in experiments to determine whether a fiber laser is single mode or not. For single-mode fiber lasers, the value of M^2 is near unity, while $M^2 > 1$ is indicative of beam contamination with higher-order modes. To calculate M^2, we adopt the variance method, which is mathematically rigorous and closely resembles the common experimental procedures for the M^2 measurement [9].

Consider an optical beam with the electric field profile $E(x, y, z)$ propagating in the z direction. The beam center $\langle x \rangle$ and the standard deviation of the intensity distribution σ_x^2 across the x coordinate are

$$\langle x \rangle(z) = \iint dSx|E(x, y, z)|^2, \tag{2-8}$$

$$\sigma_x^2\,(z) = \iint dS(x - \langle x \rangle(z))^2|E(x, y, z)|^2. \tag{2-9}$$

Since we consider only cylindrically symmetric optical fibers, the results are identical for the y coordinate, and we take the liberty of dropping the x subscript (e.g.,M^2) when convenient. It can be shown that the standard deviation in Eq. (2-9), in the paraxial approximation, obeys a universal free-space propagation rule of the form

$$\sigma_x^2\,(z) = \sigma_x^2\,(z_0) + A\frac{\lambda}{2\pi}(z - z_0) + B\frac{\lambda^2}{4\pi^2}(z - z_0)^2. \tag{2-10}$$

z_0 is the coordinate of the output facet of the fiber, which does not necessarily coincide with the position of the beam waist. Reference [8] has shown that

$$A = \iint idS\big(x - < x > (z_0)\big)[E\,\frac{\partial E^*}{\partial x} - c.c], \tag{2-11}$$

$$\text{B}=\iint dS\left|\frac{\partial E}{\partial x}\right|^2 + \frac{1}{4}\left[\iint dS(E\,\frac{\partial E^*}{\partial E} - c.c)\right]^2, \tag{2-12}$$

where $E \equiv E(x, y, z_0)$ is implied in Eqs. (2-11) and (2-12) and $c.c$ is complex conjugate of $\frac{\partial E^*}{\partial E}$. The position of the beam waist $\tilde{z}_{0x}$ and the beam-quality factor M_x^2 are given by

$$\tilde{z}_{0x} = z_0 - \pi A/(\lambda B), \tag{2-13}$$

$$M_x^2 = \sqrt{4B\sigma_x^2(z_0) - A^2}. \tag{2-14}$$

We note that we slightly differ with [8] in the sign of the frequency term and also the definition of the A term. While the integrals for the M^2 parameter can be evaluated numerically, one is faced with the challenge of reliably truncating the infinite integrals. It is difficult to choose a reliable truncation radius, $a\ priori$, for a desired error. Therefore, a closed-form analytical expression is preferable. Using the parameters defined in Eqs. (2-15) and (2-16),

$$\zeta_{n:u}^m = (u^2 + u^{*2})^m/(u^2 - u^{*2})^n, \tag{2-15}$$

$$\gamma = uJ_1(u)/J_0(u)\ , \tag{2-16}$$

$\widetilde{N}$, A, B can be expressed as

$$(4\pi a^2\widetilde{N}^2)^{-1} = i(\zeta_{1:u}^0 + \zeta_{1:w}^0).Im(\gamma), \tag{2-17}$$

$$(\pi a^2\widetilde{N}^2)^{-1}A = -4(\zeta_{2:u}^1 + \zeta_{2:w}^1).Im(\gamma) - i(\zeta_{1:u}^1 + \zeta_{1:w}^1) - 2i(\zeta_{1:u}^0 + \zeta_{1:w}^0).|\gamma|^2, \tag{2-18}$$

$$(2\pi\widetilde{N}^2)^{-1}B = Re[(u^{*2}\zeta_{1:u}^0 - w^{*2}\zeta_{1:w}^0).\gamma], \tag{2-19}$$

$$\left(\pi a^4\widetilde{N}^2\right)^{-1}\sigma_x^2(z_0) = -8i(\zeta_{3:u}^1 + \zeta_{3:w}^1).Im(\gamma) + \left(2\pi a^2\widetilde{N}^2\right)^{-1} + 2(\zeta_{2:u}^1 + \zeta_{2:w}^1) +$$

$$4(\zeta_{2:u}^0 + \zeta_{2:w}^0).|\gamma|^2. \tag{2-20}$$

2.3 Results and Discussion

The contour plots of M^2 as a function of ΔN and G are shown in Figs. (2-1)-(2-3).

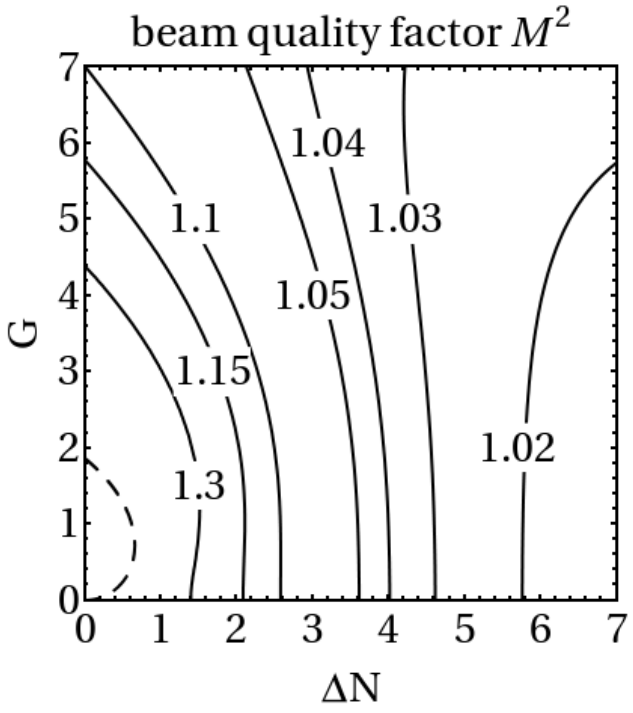

Fig. (2-1). Contour plot of M^2 as a function of ΔN and G in the $GG - IG$ region.

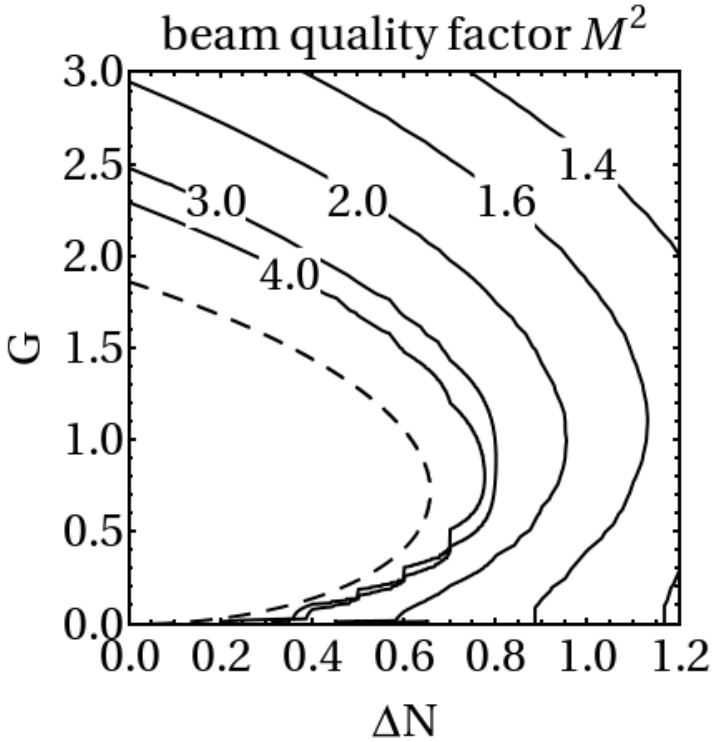

Fig. (2-2). Contour plot of M^2 as a function of ΔN and G in the $GG - IG$ region but zoomed in near the origin.

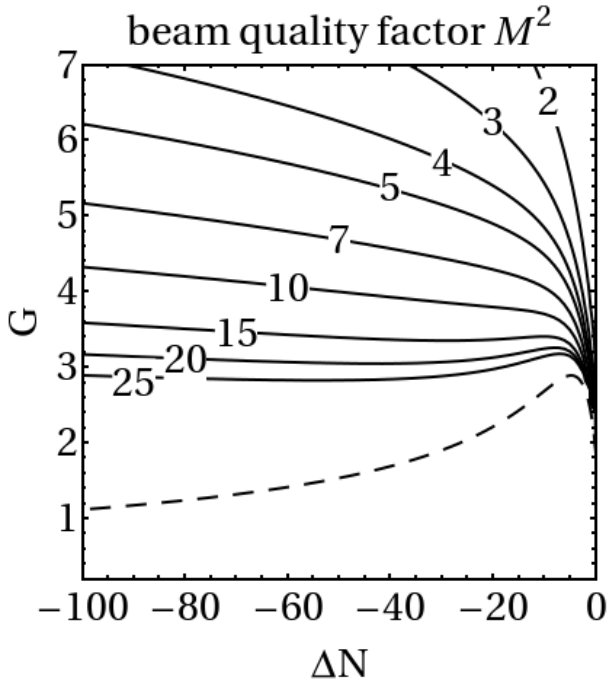

Fig. (2-3). Contour plot of M^2 as a function of ΔN and G in $GG - IAG$ region. The dashed lines represent the LP_{01} guiding threshold.

The dashed lines in these figures identify the threshold values of the dimensionless gain parameter G required to produce a confined and amplifying LP_{01} mode as described in [1]. The results in Fig. (2-1), related to the $GG - IG$ region, show that M^2 remains very close to unity over most of the parameter space. A typical single-mode fiber laser operates at $4 \leq \Delta N \leq 6$, for which $M^2 \leq 1.04$, regardless of the value of the G parameter. This is consistent with the common intuition that the beam quality of a single-mode fiber laser is very good and does not degrade by pumping unless higher-order modes are excited. However, the beam quality factor rapidly increases as the $\tilde{V}$ parameter of the fiber gets closer to the (dashed line) LP_{01} threshold. This can be seen in Fig. (2-2), which is similar to Fig. (2-1) but zoomed in near the origin and the close proximity of the LP_{01} threshold line.

The situation is quite different in the $GG-IAG$ region, as shown in Fig. (2-3). M^2 is quite large over the entire parameter space and becomes exceptionally large near the (dashed line) LP_{01} threshold. The large value of M^2, especially near the threshold, is the result of the long tail of the beam intensity extending all the way into the cladding region over a large portion of the $GG-IAG$ parameter space [6]. The situation closely resembles the case of a conventional IG fiber ($G=0$), where the tails of the beam extend to the cladding in the weakly guiding limit of $\Delta \rightarrow 0$, resulting in large values of M^2 as shown in Fig. (2-2). We note that the numerical evaluation of M^2 becomes increasingly difficult in the regions of large M^2, and proper care must be taken in the sampling and truncation of the beam to get an accurate result.

To explore the impact of the long intensity tail in the cladding on the value of M^2, we introduce a Gaussian apodization function of the form $\exp(-\alpha^{-1}r^2/a^2)$ to softly truncate the long intensity tail of beam. We multiply the beam profile of Eq. (2-4) by the apodization function and calculate the M^2 numerically. The results are presented in Fig. (2-4), where M^2 is plotted as a function of G for $\Delta N=1000$ (solid line) and $\Delta N=-100$ (dotted line). For each value of ΔN, two lines are plotted for $\alpha=2$, 8 from the apodization function, and one line for $\alpha=\infty$, which is in the absence of the apodization function. Fig. (2-4) clearly shows that the truncation of the intensity tail of the $GG-IAG$ beam results in a substantial reduction in the calculated value of M^2.

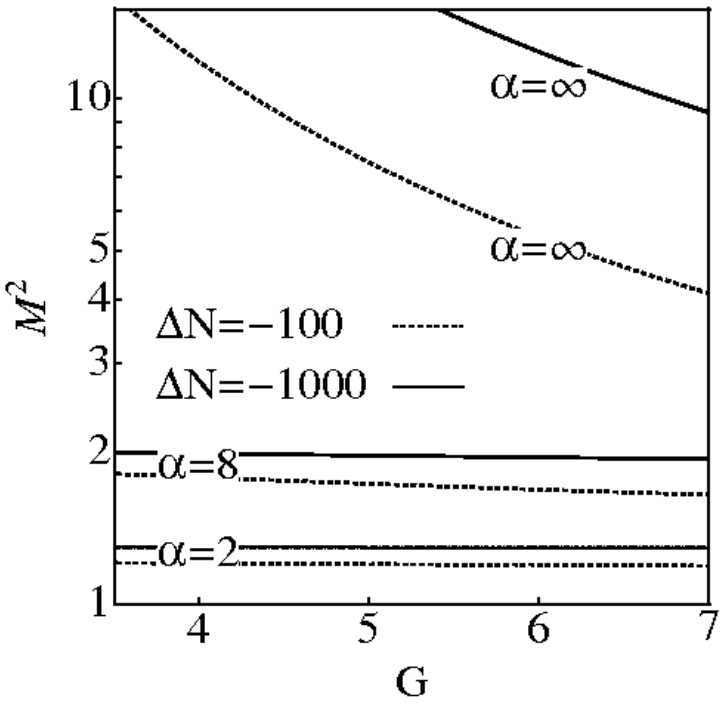

Fig. (2-4). Contour plot of M^2 as a function of ΔN and G in the M^2 as a function of G for $\Delta N = -1000$ (solid lines) and $\Delta N = -100$ (dotted lines). The lines relate to the apodized beam and are marked by different values of α from the apodization function.

These observations are quite important in relating the M^2 values reported in this chapter, especially for the $GG - IAG$ region of Fig. (2-3) to the experimental measurements. In practice, the extended tail of the $GG - IAG$ beam is truncated at the cladding-jacket (or cladding-air) interface. For example, for $\Delta N = -100$ and G equal to twice the LP_{01} threshold value, the field amplitude drops by only 25% from $r = a$ to $r = 2a$; for $\Delta N = -1000$, this drop in amplitude is only 13%. Therefore, the impact of the cladding-jacket interface on the tail of beam warrants close attention.

We expect that very large values of M^2 will be observed in GG − IAG single-mode fibers with sufficiently large cladding to core diameter ratios. Measurement of M^2 can be challenging for these fibers, since the presence of noise can impact an accurate assessment of the tail intensity. The existing experiments [2–5] deviate from the pure

GG − IAG formalism of Siegman [1] in the sense that the cladding-core diameter ratios are not sufficiently large. Therefore, an accurate M^2 comparison with these experiments is possible only if the presence of the cladding-jacket interface is explicitly taken into account. Since the cladding-to-core ratio is likely to remain small in practical GG − IAG designs, a detailed analysis of the impact of the cladding truncation on M^2 is warranted. Besides the impact on the value of M^2, one must examine whether the truncated mode remains faithful to its GG − IAG nature or is modified into a mode that is primarily index guided by the cladding-jacket index step. In chapter 3, we will study the impact of truncation of the beam profile on M^2 at the cladding-jacket interface.

2.4 References

[1] A. E. Siegman, "Propagating modes in gain-guided optical fibers," J. Opt. Soc. Am. A 20, 1617-1628 (2003).

[2] A. E. Siegman, Y. Chen, V. Sudesh, M. C. Richardson, M. Bass, P. Foy, W. Hawkins, and J. Ballato, "Confined propagation and near single mode laser oscillation in a gain guided, index antiguided optical fiber," Appl. Phys. Lett. 89, 251101 (2006).

[3] T. McComb, V. Sudesh, Y. Chen, M. Bass, M. C. Richardson, J. Ballato, and A. E. Siegman, "Single Mode Lasing in a 200m Diameter Core Gain-guided Index Anti-guided Diode End Pumped Fiber," in Lasers and Electro-Optics Society, 242-243 (2007).

[4] Y. Chen, V. Sudesh, T. McComb, M. C. Richardson, M. Bass, and J. Ballato, "Lasing in a gain-guided index antiguided fiber," J. Opt. Soc. Am. B 24, 1683 (2007).

[5] Y. Chen, T. McComb, V. Sudesh, M. C. Richardson, and M. Bass, "Very large-core, single-mode, gainguided, index-antiguided fiber lasers," Opt. Lett. 32, 2505 (2007).

[6] A. E. Siegman, "Gain-guided, index-antiguided fiber lasers," J. Opt. Soc. Am. B 24, 1677 (2007).

[7] A. Mafi and J. V. Moloney, "Beam Quality of Photonic-Crystal Fibers," J. Lightwave Technol. 23, 2267 (2005).

[8] H. Yoda, P. Polynkin, and M. Mansuripur, "Beam Quality Factor of Higher Order Modes in a Step-Index Fiber," J. Lightwave Technol. 24, 1350 (2006).

[9] T. F. Johnston, "Beam Propagation (M^2) Measurement Made as Easy as It Gets: The Four-Cuts Method," Appl. Opt. 37, 4840 (1998).

Chapter 3

Beam Quality Factor of Single Mode Gain Guided Index Anti guided Fiber Lasers With Finite Cladding Boundary

3.1 Introduction

It is highly desirable to increase the core size of single-mode fiber lasers and amplifiers. A large core diameter can help mitigate unwanted nonlinear optical effects, raise the optical damage threshold, and increase the amplification per unit length of the fiber [1]. Siegman [2, 3] has recently shown that gain-guided, index-antiguided (GG-IAG) fibers can operate in a robust single transverse mode, even for arbitrarily large core diameters. Since then, several experiments have demonstrated GG-IAG in various fiber laser configurations [4–8]. Single mode operation in optical fibers with unprecedented core diameters of larger than 200 μm has been observed.

In his landmark papers, Siegman carried out a comprehensive analysis of GG-IAG fibers, assuming an infinite diameter for the cladding [2, 3]. While the infinite cladding is an acceptable approximation in conventional single-mode index guiding (IG) fibers, we suggest that the finiteness of the cladding diameter can have a considerable impact of the physical characteristics of the propagating beam in GG-IAG fibers and related experimental measurements. There are two main reasons for the inadequacy of the infinite-cladding approximation. One is that, due to practical limitations on the total diameter of the fiber and because of the extremely large core sizes, all existing experiments [4–8] report an unusually small ratio of the cladding to core diameter. Another is that the GG-IAG mode, characteristically, can have a very long and slowly decaying intensity profile in the cladding, extending all the way to the outer boundary of the cladding. For example, we recently showed the inadequacy of the infinite cladding approximation in predicting the beam quality measurements in various experiments on GG-IAG fibers [9].

Since the cladding-to-core-diameter ratio is likely to remain small in practical GG-IAG designs, a detailed analysis of the impact of the cladding truncation on these fibers is warranted. In this paper, we build upon the results of Siegman in [2,3] and extend his work to the case where the cladding of the GG-IAG fiber has a finite diameter and is truncated by a jacket. The jacket is assumed to be infinite and can be a polymer or glass protective layer on the cladding, or simply air. We explore the implications of the finite cladding diameter in detail in this chapter and illustrate its main similarities and differences with the case of infinite cladding (IC) diameter. In particular, we show that a reliable comparison with the beam quality M^2 measurements in recent experiments is only possible if the presence of the cladding–jacket interface is explicitly taken into account.

In subsection 3.2.1, we will present a brief overview of the GG-IAG fibers, for the ideal case where the cladding extends to infinity. In subsection 3.2.2, we extend the formalism to the case of finite cladding. The results will be used in sections 3.3 and 3.4 to study the impact of finite cladding on the beam profile and beam quality of GG-IAG optical fibers, respectively. We will conclude in section 3.5. Finally, in appendix A, we will report on an analytical derivation of the M^2 in GG-IAG fibers that was derived by Dr. Krishna Mohan Gundu in our group, and we compared and confirmed his analytical results with our numerical calculation. Proper care has been taken in choosing a notation that conforms with that of Siegman [3] in order to clearly illuminate the transition from the finite-cladding formulation to the limiting case of the infinite cladding.

3.2 General Characteristics

3.2.1 GG-IAG Fiber with Infinite Cladding .

In the presence of gain, an ideal (GG-IG or GG-IAG) step-index optical fiber with infinite cladding can be characterized by a generalized complex V parameter squared [2] defined as

$$\tilde{V}_{12}^2 = \Delta N + iG, \tag{3-1}$$

The index and gain parameters ΔN and G are given by

$$\Delta N = \left(\frac{2\pi a}{\lambda}\right)^2 (2\mathrm{n}_0 \Delta n), \tag{3-2}$$

$$G = \left(\frac{2\pi a}{\lambda}\right)^2 (\frac{n_0 \lambda}{2\pi})\mathrm{g}, \tag{3-3}$$

where n_2 is the refractive index of the cladding. $n_1 = n_2 + \Delta n$ is the refractive index of the core, a is the core radius, g is core power-gain coefficient, and λ is the vacuum wavelength. ΔN is negative for an IAG fiber. For a proper choice of ΔN and G, Siegman [2] has shown that the core can support an LP_{01} guided mode in the form of

$$E(x, y, z_0) = \begin{cases} N \frac{J_0(u_1 r/a)}{J_0(u_1)}, & r \le a \\ N \frac{K_0(u_2 r/a)}{K_0(u_2)}, & r > a \end{cases} \tag{3-4}$$

$\widetilde{N}$ is an overall constant to be determined from the normalization condition Eq. (3-5) assumed throughout this paper,

$$\iint dS |E(x, y, z)|^2 = 1 \tag{3-5}$$

Where $\iint dS = \iint dxdy$. The complex modal parameters u_1 and u_2 are defined as

$$u_1^2 = (n_1^2 k_0^2 - \beta^2) a^2 \tag{3-6}$$

$$u_2^2 = (\beta^2 - n_2^2 k_0^2) a^2 \tag{3-7}$$

where β is the propagation constant of the propagating mode and $k_0 = 2\pi/\lambda$. The modal parameters are related to the V number as

$$u_1^2 + u_2^2 = \tilde{V}_{12}^2 = \Delta N + iG \tag{3-8}$$

The dispersion Eq. (3-9) is obtained from matching the electric field and its slope at the core–cladding interface:

$$\frac{u_1 J_1(u_1)}{J_0(u_1)} = \frac{u_2 K_1(u_2)}{K_0(u_2)} \tag{3-9}$$

Eqs (3-8) and (3-9) can be used to determine u_1 and u_2, given $\tilde{V}_{12}$. In general, the value of $\tilde{V}_{12}$determines the total number of confined guided modes in the fiber in the presence of gain, which can be zero or higher. We note that a confined propagation mode must decay exponentially in the radial direction in the cladding. This condition requires the complex modal parameter u_2 to have a positive real value $[\Re(u_2) > 0]$. Those solutions of Eqs. (3-8) and (3-9) that satisfy $\Re(u_2) < 0$ are the leaky modes that grow exponentially to infinity in the transverse direction in the cladding. In the complex plane of $(\Delta N, G)$ shown in Fig. (3-1), $\Re(u_2) = 0$ serves as the threshold line between confined and leaky modes and is portrayed as a solid line.

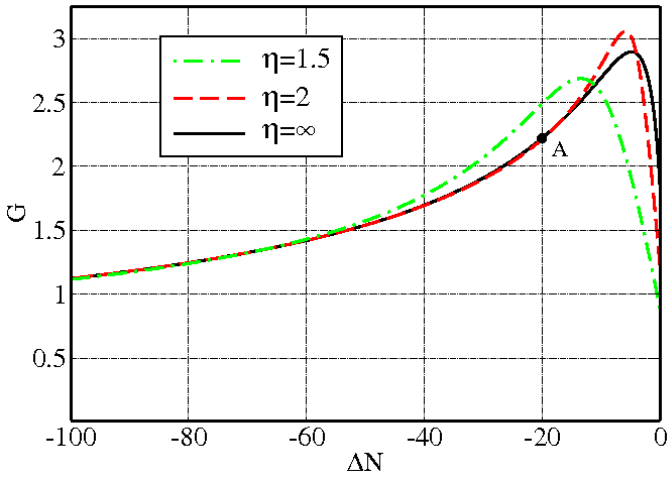

Fig. (3-1). The lines represent, $\Re(u_2) = 0$ for the case of IG-GG fibers ($\eta = \infty$) and FC-GG fibers ($\eta = 2, 1.5$). For $\eta = \infty$, the solid line serves as the mode boundary threshold separating the LP_{01} guiding modes from the leaky modes in the complex $(\Delta N, G)$ plane.

The confined guiding modes are related to the points above the solid threshold line, while the leaky modes relate to the points below the threshold line. Here and throughout this

chapter we restrict our studies to the more interesting IAG region where $\Delta N < 0$, since the properties of the IG region where $\Delta N > 0$ are not much different from a conventional optical fiber in the absence of gain.

3.2.2 GG-IAG Fiber with Finite Cladding

In this subsection, we generalize the formulation of GG optical fibers presented in Subsection 3.2.1 to the case where the cladding has a finite radius b. The refractive index profile of the finite-cladding GG (FC-GG) fiber is given by

$$n(x) = \begin{cases} n_1 & r \le a \\ n_2 & a < r \le b \\ n_3 & b < r \end{cases} \tag{3-10}$$

n_3 is the refractive index of the medium surrounding the cladding, referred to as the jacket. The electric field profile of the LP_{01} core guided mode can be generally expressed as

$$E(x, y, z_0) = \begin{cases} \widetilde{N} \frac{J_0(u_1 r/a)}{J_0(u_1)} & r \le a \\ \widetilde{N} \frac{L_0(u_2 r/a)}{L_0(u_2)} & a < r \le b \\ \widetilde{N} \frac{L_0(u_2 \eta)}{L_0(u_2)} \frac{K_0(u_3 r/a)}{K_0(u_3)} & b < r \end{cases} \tag{3-11}$$

$\widetilde{N}$ is an overall constant to be determined from the normalization condition Eq. (3-5). We have also defined

$$L_0(x) = K_0(x) + (\tfrac{S_2}{S_1}) J_0(x) \tag{3-12}$$

$\eta = b/a$ is the ratio of the radius of the cladding to the radius of the core, and S_1 and S_2 are defined in Eqs. (3-13) and (3-14):

$$S_1 = u_1 J_0(u_2) J_1(u_1) - u_2 J_0(u_1) J_1(u_2) \tag{3-13}$$

$$S_2 = u_2 J_0(u_1) K_1(u_2) - u_1 K_0(u_2) J_1(u_1) \tag{3-14}$$

u_1, u_2, and u_3 are the modal parameters in the core, cladding, and the outer layer, respectively. u_1 and u_2 are defined in Eqs. (3-6) and (3-7), while u_3 is defined in Eq. (3-15):

$$u_3^2 = (\beta^2 - n_3^2 k_0^2) b^2 \tag{3-15}$$

The continuity of the field and its first derivative across the boundaries, $r = a$ and $r = b$, results in the following dispersion relation:

$$(\eta \frac{u_2}{u_3}) \frac{S_1 K_1(u_2\eta) + S_2 J_1(u_2\eta)}{S_1 K_0(u_2\eta) + S_2 J_0(u_2\eta)} = \frac{K_1(u_3)}{K_0(u_3)} \tag{3-16}$$

We can also define a new V parameter ($\tilde{V}_{23}$) to characterize the index step at the cladding–jacket interface:

$$\tilde{V}_{23}^2 = \left(\frac{2\pi a}{\lambda}\right)^2 (n_2^2 - n_3^2) = (\frac{u_3}{\eta})^2 - u_2^2 \tag{3-17}$$

For IG-GG fibers in subsection 3.2.1, all the information required to determine u_1 and u_2, and therefore the mode field profile, was encoded in a single dimensionless complex parameter $\tilde{V}_{12}$. In the case of FC-GG fibers, in addition to $\tilde{V}_{12}$, we also need the values of the dimensionless parameters $\tilde{V}_{23}$ and η in order to determine u_1, u_2, and u_3, required for the mode profile. Equations (3-8), (3-16), and (3-17) will be used to solve for the modal parameters, given the values of $\tilde{V}_{12}$, $\tilde{V}_{23}$, and η.

3.3 Mode Profile in an FC-GG Fiber

The formulation we presented in section 3.2 is applicable in general to any selection of complex values for the refractive indexes of the core, cladding, and jacket. However, we focus our analysis on the case where the cladding and jacket are not active, so n_2 and n_3 are assumed to be real throughout this chapter. This practical choice conforms to the assumptions of [3] and also the subsequent experimental studies of GG-IAG optical

fibers. We also note that, for simplicity, we choose the jacket to be made of air ($n_3 = 1$) to carry out our analysis. However, we will comment on other choices for the jacket material.

The electric field profile of the LP_{01} mode for the case of an IG-GG fiber was analyzed in detail by Siegman [3]. In Fig. 3.2, we present the amplitude of the electric field profiles for a generic example where $\Delta N = -20$, for the case of infinite cladding ($\eta = \infty$), as well as for three cases of FC diameters, characterized by $\eta = 3, 2, 1.5$. In each case, the amplitude of the LP_{01}mode is plotted for three values of gain $G = 2G_{th}$ (solid), $G = G_{th}$ (dashed), and $G = 0$ (dotted–dashed). Point A, marked on Fig. (3-1), represents $\Delta N = -20$ and $G = G_{th}$, for the IC case. We note that we use an identical value of G_{th} at $\Delta N = -20$ as evaluated for IC-GG fibers for all four plots, since the concept of a guidance threshold might be meaningless in FC-GG fibers, as will be argued later in this section.

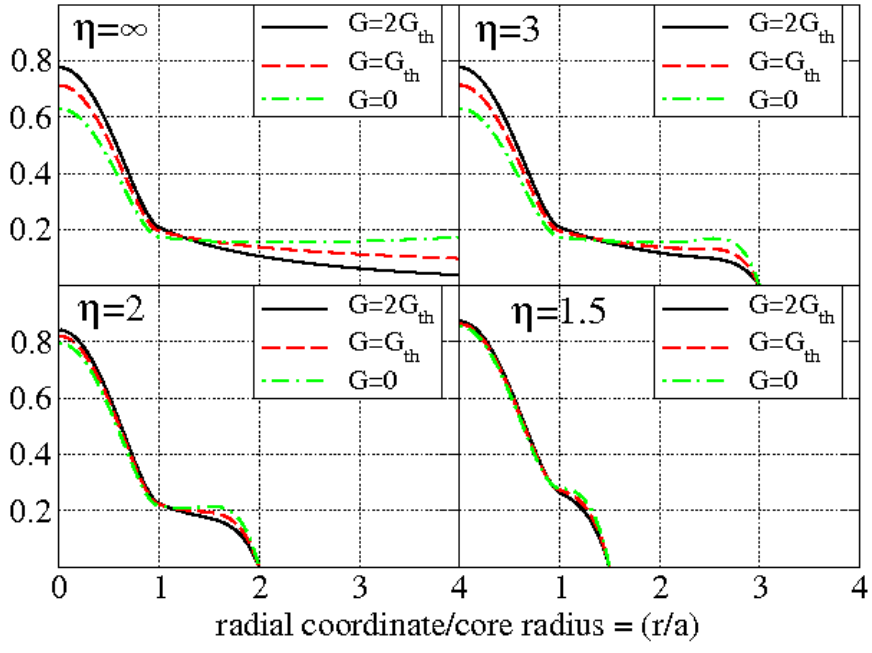

Fig. (3-2). Electric field profiles for the case of $IC - GG$ fibers ($\eta = \infty$) in the top-left graph and FC-GG fibers ($\eta = 3, 2, 1.5$) in the other three graphs.

We first recall the behavior of the field profile for infinite cladding (η = ∞). The point characterized by $G = 2G_{th}$ belongs to the parameter region $G > G_{th}$, generally associated with an intensity tail in the cladding, which drops exponentially in the radial direction. As the gain parameter (G) approaches the threshold value (G_{th}), the tail extends farther into the cladding and the rate of exponential decay slows down. At $G = G_{th}$, the tail reaches a finite nonzero asymptotic value at infinity. For $G < G_{th}$, including $G = 0$, the cladding tail grows exponentially into the cladding region and the field turns into a leaky mode. This behavior is clearly observed in the top-left of Fig. (3-2).

We now investigate the LP_{01} field profiles for the cases of finite cladding: $\eta = 3$, $\eta = 2$, and $\eta = 1.5$, presented in the top-right, bottom-left, and bottom-right of Fig. (3-2), respectively. We expect that the electric field profile of an LP_{01} mode in an FC-GG fiber to somewhat resemble that of an IC-GG fiber in the core and the cladding. The profiles in Fig. (3-2) show that this expectation holds true and is most accurate for large values of η, such as $\eta = 3$. The most notable departure of the field profiles of the FC-GG fibers from that of IC-GG is the strong truncation of the intensity tail at the cladding–jacket interface, due to the large index step. For $G \leq G_{th}$, the truncation has a greater impact on the profile of the mode in the core and in the cladding, compared with $G > G_{th}$. The impact is also greater for smaller values of η, as expected. We note that, except for the case of $\eta = \infty$, all the mode profiles plotted in Fig. (3-2) satisfy the normalization condition of Eq. (3-5), if the vertical axes in Fig. 2 are to be regarded in units of $(1/a)$. However, since the two cases of $G = 0$ and $G = G_{th}$ are not normalizable for $\eta = \infty$ in the top-left

of Fig. (3-2), we scaled all the profiles belonging to $\eta = \infty$ to match that of η = 3 at the origin (r = 0) for easier comparison.

Another important point for FC-GG profiles is that the truncation at the cladding–jacket interface turns leaky modes into proper normalizable guided modes. In other words, unlike the IC-GG fiber, $\Re(u_2) = 0$ no longer serves as a GG threshold for FC-GG fibers. We note that the normalizability requirement that imposed a condition of $\Re(u_2) > 0$ on the guided modes of IC-GG fibers is now replaced by $\Re(u_3) > 0$ for $FC - GG$ fibers. Those solutions of Eqs. (3-8), (3-17), and (3-16) that satisfy $\Re(u_3) < 0$ are the leaky modes that grow exponentially to infinity in the transverse direction in the jacket. In the next paragraph, we will argue that, for a sufficiently large refractive index contrast between the cladding layer and the jacket, it is possible for all FC-GG modes defined on the complex plane of $(\Delta N, G)$ to be guiding. In other words, the condition $\Re(u_3) = 0$ may no longer translate into a guiding threshold on this complex plane, and there will be no leaky LP_{01}-like modes. However, for finite values of η, it might be interesting to find the quasi-threshold line of $\Re(u_2) = 0$. This quasithreshold lines are plotted in Fig. (3-1) for $\eta = 2$ and $\eta = 1.5$ as dashed and dotted–dashed, respectively. A quasi-threshold line for $\eta > 3$ becomes virtually indistinguishable from the solid threshold line ($\eta = \infty$) belonging to IC-GG fibers in Fig. (3-1). We emphasize again that the quasi-threshold lines are for illustration purposes and do not present any physical threshold for guiding versus leaky properties in FC-GG fibers.

We now argue that $\Re(u_3) = 0$ may no longer translate into a guiding threshold. In practice, there is an often large refractive index contrast between the cladding layer and

the jacket, especially if the jacket is assumed to be air (our choice in this paper). Therefore, $\tilde{V}_{23}$ can be quite large. Using Eq. (3-17) and assuming $\tilde{V}_{23} \gg |u_2|$, we get

$$\Re(u_3) \approx \eta\tilde{V}_{23}(1-\frac{\Im(u_2)^2-\Re(u_2)^2}{2\tilde{V}_{23}^2} + O(\tilde{V}_{23}^{-4})) \quad (3\text{-}18)$$

It is clear that, unless, $\Re(u_3)$ remains positive and the mode is confined. Therefore, unlike the IC-GG fibers, guided modes exist even below the solid-line threshold of Fig. (3-1). We note that, for all three choices of η studied in this paper, the values of the modal parameters u_1 and u_2 are almost the same in IC-GG and FC-GG fibers. Therefore, u_1 and u_2 as the numerical solutions of the much simpler IC-GG dispersion Eq. (3-9) can be used as a starting point in the search algorithm to find u_1, u_2, and u_3 in the case of FC-GG fibers. For our choice of parameters, $\eta = 3$ is practically identical to $\eta = \infty$ when it comes to solving for u_1 and u_2 for the root-finding algorithm we employed in Mathematica. We note that, solving for the modal parameters, using the dispersion equation of the FC-GG fibers becomes increasingly harder as η gets larger.

Last, we would like to comment on our choice of $n_3 = 1$. Our observations reported in this chapter should hold true as long as n_2 and n_3 are not too close. On the other hand, in the limit of $n_3 = n_2$, the FC-GG fiber becomes identical to the IC-GG case. In terms of using a root-finding algorithm with u_1 and u_2 from IC-GG fibers as the seed for the FC-GG case, our choice of $n_3 = 1$ is the most stringent choice and larger values of n_3 will result in even greater resemblance between the LP_{01} profiles and modal parameters in IC-GG and FC-GG fibers

3.4 Beam Quality Factor in an FC-GG Fiber

The reported values of the beam quality factor M^2 in several experiments [4–8] are notably larger than unity, in the range of $1.05-2.0$, even in fibers that are designed to

operate as single mode. This should not be surprising considering the substantial departure of the LP_{01} profile of a GG-IAG fiber from a Gaussian-like beam, as similarly reported in other unconventional optical fibers [10]. We conducted an extensive theoretical study of the beam quality factor M^2 of single-mode fibers in the presence of gain [9]. We showed that the theoretical predictions of the M^2 in the GG-IAG region can be substantially larger than the experimental measurements ($M^2 > 10$) and attributed this difference to the truncation of the long tail of the beam extending all the way into the cladding region in the experiments, which can lower M^2 substantially. For example, [4] reports $M^2 \leq 2$ for a GG-IAG optical fiber with a 100 μm core diameter and a 250 μm cladding diameter. Similarly, [5] reports $1.2 \leq M^2 \leq 1.5$, where the core and cladding diameters are 200 and 340 μm, respectively. Reference [8] reports $M^2 \approx 1.4$ for a $GG - IAG$ optical fiber with a 100 μm core diameter and a 250 μm cladding diameter. The cladding diameter is not much larger than the core diameter in either experiment. Therefore, it is not surprising that these experiments measure such low values of M^2.

In order to explore the impact of the long intensity tail in the cladding on the value of M^2 in [9], we introduced a Gaussian apodization to softly truncate the long intensity tail of the beam calculated from an IC-GG fiber. Although this served as a reasonable and convenient approximation, the mode profiles plotted in Fig. (3-2) show that a more rigorous study is warranted. For example, a simple Gaussian field truncation at the cladding–jacket boundary for $\eta = 1.5$ does not seem to be an adequate approximation. Our method for calculating the M^2 is similar to that reported in [9]. Consider an optical beam with the electric field profile $E(x, y, z)$ propagating in the z direction. The beam

center $\langle x \rangle$ and the standard deviation of the intensity distribution σ_x^2 across the x coordinate are

$$\langle x \rangle(z) = \iint dSx|E(x,y,z)|^2 \tag{3-19}$$

$$\sigma_x^2\,(z) = \iint dS(x - \langle x \rangle(z))^2|E(x,y,z)|^2 \tag{3-20}$$

Since we only consider cylindrically symmetric optical fibers, the results are identical for the y coordinate, and we take the liberty in dropping the x subscript (e.g., M^2) when convenient. It can be shown that the standard deviation in Eq. (3-20), in the paraxial approximation, obeys a universal free-space propagation rule of the form

$$\sigma_x^2\,(z) = \sigma_x^2\,(z_0) + A\frac{\lambda}{2\pi}(z - z_0) + B\frac{\lambda^2}{4\pi^2}(z - z_0)^2 \tag{3-21}$$

z_0 is the coordinate of the output facet of the fiber, which does not necessarily coincide with the position of the beam waist. Reference [11] has shown that

$$A = -i \iint dS\big(x - < x > (z_0)\big)[E\frac{\partial E^*}{\partial x} - c.c] \tag{3-22}$$

$$\text{B}=\iint dS\left|\frac{\partial E}{\partial x}\right|^2 + \frac{1}{4}\left[\iint dS(E\frac{\partial E^*}{\partial E} - c.c)\right]^2 \tag{3-23}$$

where $E \equiv E(x,y,z)$ is implied in Eqs. (3-22) and (3-23). The position of the beam waist $\tilde{z}_{0x}$ and the beam quality factor M_x^2 x are given by

$$\tilde{z}_{0x} = z_0 - \pi A/(\lambda B) \tag{3-24}$$

$$M_x^2 = \sqrt{4B\sigma_x^2(z_0) - A^2}. \tag{3-25}$$

We note that we slightly differ with [11] in the sign of the frequency term and also the definition of the A term. Our definitions remain consistent with [9], except for a missing minus sign in the definition of A, which has been corrected here in Eq. (3-22). For the case of finite cladding, we consider the generic electric field profile of Eq. (3-11). While

the value of M^2 in Eq. (3-25) can be evaluated numerically, we also derive a closed-form analytical expression for the M^2 parameter in Appendix A.

The contour plots of M^2 as a function of ΔN and G are shown in Figs. (3-3). Fig. (3-3a) relates to $\eta = \infty$ representing the IG-GG-IAG fibers. The dashed line in Fig. (3-3a) identifies the threshold values of the dimensionless gain parameter G required to produce a confined and amplifying LP_{01} mode as also shown in the form of a solid line in Fig. (3-1). Figs. (3-3b – 3-3d) relate to $\eta = 3$, $\eta = 2$, and $\eta = 1.5$, respectively, representing different FC-GG-IAG fibers.

The results in Fig. (3-3a), related to the GG-IAG region of FC-GG fibers, show that M^2 is quite large over the entire parameter space and becomes exceptionally large near the (dashed) LP_{01} threshold. The large value of M^2 especially near the threshold is the result of the long tail of the beam intensity extending all the way into the cladding region [9]. The situation is quite different for FC-GG fibers as shown in Figs. 4-6. The truncation of the beam tail at the cladding–jacket interface results in a substantial reduction in the calculated value of M^2. The above observations are quite important in relating the M^2 values reported in this paper to the experimental measurements.

We note that, in the $GG - IAG$ region ($\Delta N < 0$), the beam quality factor M^2 increases as $|\Delta N|$ becomes progressively larger. This trend can be observed in Figs. (3-3b – 3-3d). Also, in each of these figures, the contour lines eventually become vertical for large enough values of $|\Delta N|$. This is almost starting to happen for $\eta = 1.5$ in Fig. (3-3d) at $\Delta N \approx -100$. For larger values of η, this effect happens at larger values of $|\Delta N|$. In other words, for very negative values of ΔN, the M^2 parameter becomes independent of the G parameter. This can be seen in Fig. (3-4), where we plot M^2 as a function of G for

$\Delta N = -100$ (left) and $\Delta N = -1000$ (right). It can also be seen that, for each of the three choices of $\eta = 1.5$ (solid), $\eta = 1.7$ (dashed), and $\eta = 1.8$ (dotted–dashed), a larger value of ΔN results in a larger beam quality factor. This is also consistent with our remarks regarding the extrapolation of Figs. (3-3b - 3-3d) to more negative values of ΔN.

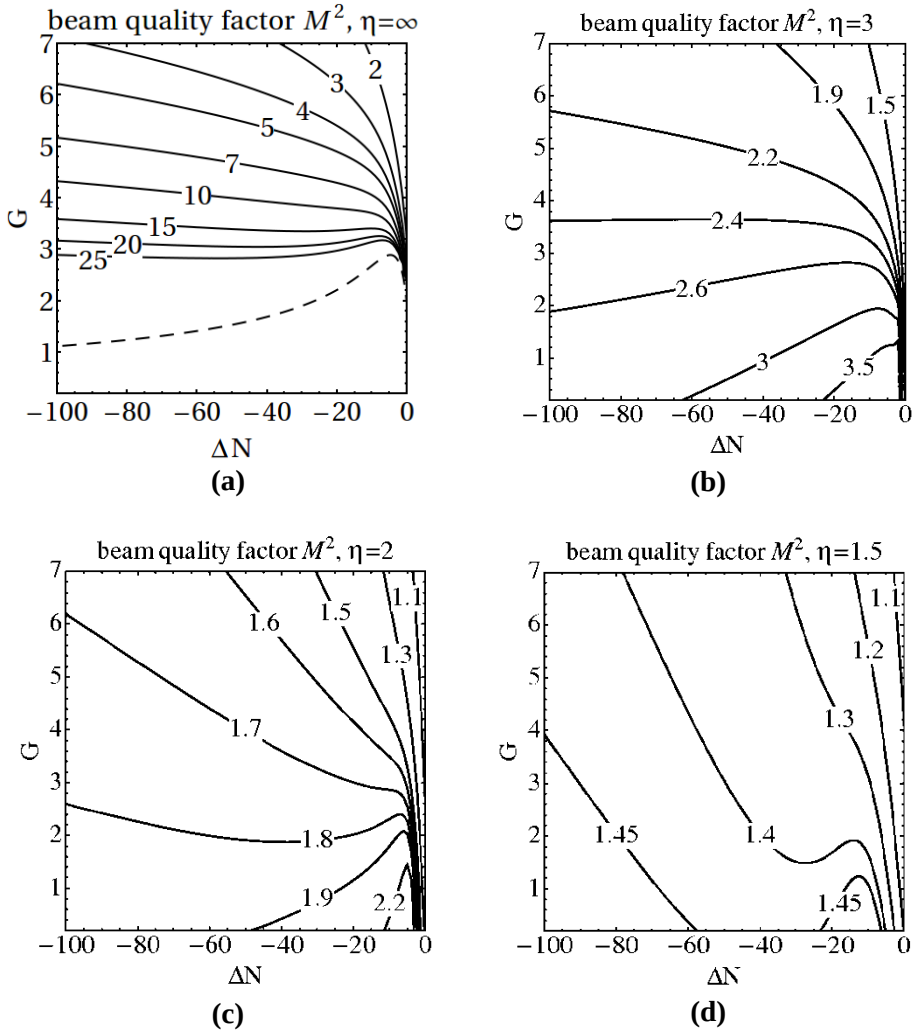

Fig. (3-3) Contour plot of M^2 as a function of ΔN and G in the $GG - IAG$ region for (a) IC-GG fibers with $\eta = \infty$, (b), (c), and (d) for $FC - GG$ fibers with $\eta = 3$, $\eta = 2$, and $\eta = 1.5$, respectively.

It can also be seen [as also shown in Figs. (3-3b - 3-3d)] that M^2 increases with the value of η. As we stated before, solving for the modal parameters u_1, u_2, and u_3 becomes exceedingly difficult for large values of η, even if we start with the modal parameters u_1 and u_2 from the much simpler IC-GG dispersion Eq. (3-9). For $\eta > 2$ and $\Delta N \ll -100$,

finding a solution to Eq. (3-16) becomes a complicated numerical problem and requires accuracy beyond the machine precision. Addressing such numerical issues is beyond the scope of this research, and we have chosen to extract the expected values of M^2 for $\eta > 2$ and $\Delta N \ll -100$ by observing the trends in our figures.

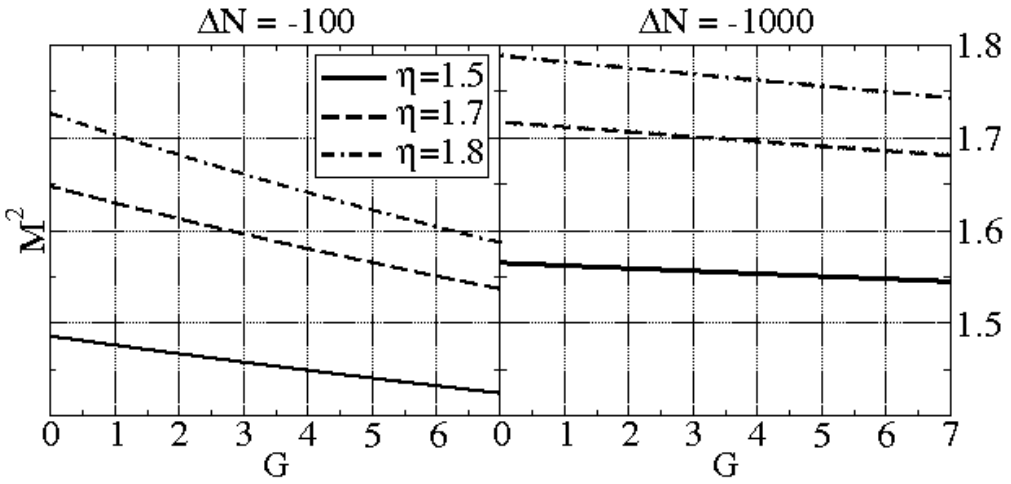

Fig. (3-4). M^2 as a function of G for (left) $\Delta N = -100$ and (right) $\Delta N = -1000$. The lines in each graph relate to the different values of $\eta =$ 1.5 (solid), $\eta =$ 1.7 (dashed), and $\eta =$ 1.8 (dotted–dashed).

3.5 References:

[1] A. Mafi, J. V. Moloney, D. Kouznetsov, A. Schülzgen, S. Jiang,T. Luo, and N. Peyghambarian, "A large-core compact high-power single-mode photonic crystal fiber laser," IEEE Photon.Technol. Lett. 16, 2595–2597 (2004).

[2] A. E. Siegman, "Propagating modes in gain-guided optical fibers," J. Opt. Soc. Am. A 20, 1617–1628 (2003).

[3] A. E. Siegman, "Gain-guided, index-antiguided fiber lasers,"J. Opt. Soc. Am. B 24, 1677–1682 (2007).

[4] A. E. Siegman, Y. Chen, V. Sudesh, M. Richardson, M. Bass,P. Foy, W. Hawkins, and J. Ballato, "Confined propagation and near single mode laser oscillation in a gain guided, index antiguided optical fiber," Appl. Phys. Lett. 89, 251101 (2006).

[5] V. Sudesh, T. McComb, Y. Chen, M. Bass, M. Richardson, J. Ballato, and A. E. Siegman, "Diode-pumped 200 μm diameter core, gain-guided, index-antiguided single mode fiber laser," Appl. Phys. B 90, 369–372 (2008).

[6] Y. Chen, V. Sudesh, T. McComb, M. Richardson, M. Bass, and J. Ballato, "Lasing in a gain-guiding index antiguided fiber," J. Opt. Soc. Am. B 24, 1683–1688 (2007).

[7] Y. Chen, T. McComb, V. Sudesh, M. Richardson, and M. Bass, "Very large-core, single-mode, gain-guiding, index-antiguided fiber lasers," Opt. Lett. 32, 2505–2507 (2007).

[8] W. Hageman, Y. Chen, X. Wang, L. Gao, G. U. Kim, M. Richardson, and M. Bass, "Scalable side-pumped, gain-guided index-anti- guided fiber laser," J. Opt. Soc. Am. A 27, 2451–2459 (2010).

[9] K. M. Gundu, P. G. Yarandi, and A. Mafi, "Beam quality factor of single-mode gain-guiding fiber lasers," Opt. Lett. 35, 4124–4126 (2010).

[10] A. Mafi and J. V. Moloney, "Beam quality of photonic-crystal fibers," J. Lightwave Technol. 23, 2267–2270 (2005).

[11] H. Yoda, P. Polynkin, and M. Mansuripur, "Beam quality factor of higher order modes in a step-index fiber," J. Lightwave Technol. 24, 1350–1355 (2006).

Chapter 4

Improving the Power Efficiency in End-Pumped Gain-Guided Index-Antiguided Fiber Amplifier

4.1 Introduction

It is highly desirable to increase the core size of high-power fiber lasers and amplifiers in order to mitigate unwanted nonlinear optical effects and raise the optical damage threshold. Conventional index-guided (IG) optical fibers become multimode for large core diameter, because it is very difficult to control and fine-tune the index step between the core and cladding to satisfy the single mode condition. Gain-guided index-antiguided (GG-IAG) fibers have been suggested by Siegman as a possible platform for ultralarge-core single-mode operation for lasers and amplifiers [1].

GG-IAG fiber has a lower refractive index in the core than in the cladding, so a sufficient amount of gain must be added to the core to help the fiber to support the guiding mode. Eqs. (4-1) and (4-2), first derived by Siegman [2], provide reliable approximations of the threshold gain required for the lossless propagation of $LP_{01}$and LP_{11}modes, respectively:

$$g_{th}^{01} = \sqrt{\frac{133.8}{2n_0^3(-\Delta n)}}\frac{\lambda^2}{4\pi^2 a^3} \tag{4-1}$$

$$g_{th}^{11} = \sqrt{\frac{862.2}{2n_0^3(-\Delta n)}}\frac{\lambda^2}{4\pi^2 a^3} \tag{4-2}$$

Here, g_{th}^{01} (g_{th}^{11}) is the minimum gain required for the LP_{01} (LP_{11}) mode to propagate without loss. The refractive index of the cladding and the core is n_0 and $n_0 - \Delta n$, respectively. λ is the signal wavelength, and a is the core radius.

Several experiments have provided the proof of concept for the single-mode operation of GG-IAG ultralarge-core fiber amplifiers and lasers [3]–[7]. All the relevant experiments have observed a stable single-mode profile at the output; however, the value of beam quality factor M^2 has been considerably larger than unity. Another common feature

among all experiments has been the rather low value for the measured output power and efficiency.

We recently studied the behavior of M^2 in GG-IAG fibers [8], [9]. We found that the value of M^2 is affected by the truncation of the slow-decaying tail of the fundamental mode at the cladding-jacket interface in GG-IAG fibers. This behavior is quite unlike that of the conventional IG single-mode fibers, where the cladding-jacket interface has virtually no impact on the profile and the beam quality factor of the guided mode. The theoretical results we obtained in [9] were consistent with the corresponding experimental observations.

The issue of low power and low efficiency of GG-IAG fiber lasers and amplifiers has also been addressed in several publications and is the main subject of these papers [3]–[7]. It has been suggested that the IAG behavior of the core at the pump wavelength prevents the pump to be efficiently absorbed in the core area. One solution to address this issue is to make the fiber IG at the pump wavelength, while keeping it IAG at the signal wavelength [6]; however, it has been challenging to find the appropriate core and cladding glass compositions with the desired dispersive behavior.

Another suggested solution has been to use Bragg confinement to increase the pump overlap with the core [10]; however, we believe that the IAG behavior at the pump wavelength has negligible impact on the pump absorption in the core of the GG-IAG fibers and a solution to the issue of low power and low slope efficiency must be looked for elsewhere. This is evidenced by the recent work of Yan et al. [11] where they numerically explore the impact of the IAG nature of the core at the pump wavelength on the absorption efficiency of the pump in the core. Although the IAG behavior affects the

pump absorption, the impact is too small to be mainly responsible for the major lack of power efficiency in reported experiments on GG-IAG fiber amplifiers and lasers. However, it must be noted that the work presented in [11], which focuses on this particular issue, is numerical and therefore depends on the assumption made in their ray-tracing-based simulations. While we suspect that the impact of the IAG structure on pump absorption is minimal for a highly multimode pumping scheme with low transverse coherence, we think that further detailed theoretical and experimental assessments of this problem are warranted in future research on GG-IAG fiber amplifiers and lasers. In the following sections, we will argue that it is the high absorption efficiency in the first few centimeters of improperly designed fiber amplifiers, which does not allow for proper pump delivery to the rest of the fiber and much of the length of the fiber attenuates the signal due to the lack of proper pumping above the required GG-IAG threshold.

Only a couple of experiments on end-pumping scheme for GG-IAG fibers have been reported so far in Nd^{+3}-doped and Yb^{+3}-doped fibers. In a pioneering study on diode-pumped GG-IAG fiber lasers, Sudesh et al. [5] observed single-mode lasing in a $200\mu m$ GG-IAG phosphate glass $L = 26\,mm$ fiber laser with 1% Nd^{+3} doping in the core. The measured lasing threshold was reported at $\approx 6W$, and the maximum output was measured to be around $9\,mW$ for larger than $20\,W$ of pump power. Sudesh et al. attributed the low slope efficiency of the laser to the IAG effect at the pump wavelength. While we think it is unlikely that IAG is having such a large impact in a multimode pumping scheme as we discussed before, considering that the fiber is also so short, we suggest that this issue can be explored by tracking the output pump power, using the cut-back method. In an ideal case where the pump is uniformly distributed across the fiber

cross section all the way along the fiber, the pump absorption in dB unit is given by $4.343 \times \eta_p N_{tot} \sigma_{12}^{(p)} L$ (approximately $3dB$ for $L = 26\,mm$), where $\sigma_{12}^{(p)} = 7 * 10^{-25} m^2$, N_{tot} is the total density of the doped Nd^{+3} ions, η_p is core area divided by the cladding area, and we have assumed low signal power as is also observed in [5]. Therefore, an absorption of much less than half ($3\,dB$) the pump power through the entire length of the fiber can be regarded as a clear signature of the lack of proper pump overlap with the core; otherwise, one must look elsewhere for the reason behind the low slope efficiency.

It may also be possible to inspect the substantial transverse signal leakage power from GG-IAG structures, depending on the experimental configuration. The gain threshold presented in Eq. (4-1) signifies a constant loss mechanism along the length of the GG-IAG fiber (due to the IAG behavior at the signal wavelength), which must be compensated by the gain provided by the amplifying medium. As such, signal power leaks sideways into the cladding or free space depending on the experimental configuration. In the experiment reported by Sudesh et al. [5], $9\,mW$ of the laser output power translates into $P = 900\,mW$ of total signal power inside the cavity (forward and backward propagating beams) near the output mirror with 98% reflectivity. Since $g_{th}^{01} \approx \frac{1.89}{m}$, we can estimate the total signal power leakage to the cladding of $g_{th}^{01} PL \approx 45mW$. Here, we have assumed constant signal power inside the cavity along the fiber, which is a fair approximation, given the high reflectivity of both mirrors, and is only valid as an order of magnitude estimation of the expected signal power leakage. Depending on the experimental configuration, this power leakage might be easily observable and can perhaps be significant in high power operations in more efficient GG-IAG fiber lasers and amplifiers to require proper safety precautions.

Side pumping has been suggested as a method to increase the efficiency of the GG-IAG fiber lasers and amplifiers. The authors of [6] and [7] suggest side-pumping to address the issue of IAG at the pump wavelength, which is claimed to negatively impact the absorption of the pump. However, side pumping has not considerably changed the low-efficiency problems associated with $GG-IAG$ structures. Moreover, side pumping is likely not suitable for scaling up the GG-IAG fiber lasers and amplifiers to longer lengths (beyond the short segments used in the proof-of-the-concept experiments) and higher powers; therefore, we focus our studies on the end-pumping scheme in this paper.

4.2 Optimum Design Criteria

In a series of experiments, Peng's group have explored Yb^{+3}-doped GG-IAG fiber amplifiers and have carried out careful experiments on the absorption of the pump [11]–[13]. While they do not directly report the Yb^{+3} doping percentages in their papers, they suggest that pump absorption is rather high in the first few centimeters of the GG-IAG fiber, leading to a large thermal load [11]. They also analyze the "negative" impact of the circular symmetry (due to nonabsorbing helical rays), and also that of the IAG structure at the pump wavelength, using a ray-tracing model [11]. However, their experiment on a D-shaped GG-IAG fiber has not improved the amplifier gain slope efficiency [13], leading one to believe that the circular symmetry may not be blamed to the poor performance of the amplifier. The authors have correctly identified the proper pump power distribution as the main performance barrier in GG-IAG fiber lasers and amplifiers. However, unlike the experiment reported on Nd^{+3}-doped GG-IAG fiber [5], the lack of pump absorption efficiency does not seem to be an issue in the reported Yb^{+3}-doped $GG-IAG$ fiber experiments [11]–[13]. Rather, it is the high absorption efficiency in the first few

centimeters of the fiber, which does not allow proper pump delivery to the rest of the fiber, and much of the length of the fiber attenuates the signal due to the lack of proper pumping above the required GG-IAG threshold. In order to see the impact of the rapid pump absorption in a Yb^{+3} -doped $GG-IAG$ fiber such as those reported by Peng's group [11], we plot the pump power and the local signal gain as a function of the length of the GG-IAG fiber ($\Delta n = -0.0045$) in Fig. (4-1). We assume 2% Yb^{+3} doping in silica fiber with core and cladding diameters of 200 and 340 μm, respectively. The input pump power is 9 W, where we have assumed uniform pump distribution across the fiber (core and cladding). Essentially, the entire pump is absorbed in the first few centimeters of the fiber; the signal is only amplified in the first $27mm$ of propagation and is attenuated afterward. The result in Fig. (4-1) clearly demonstrates the need for proper distribution of the pump power in GG-IAG fiber amplifiers.

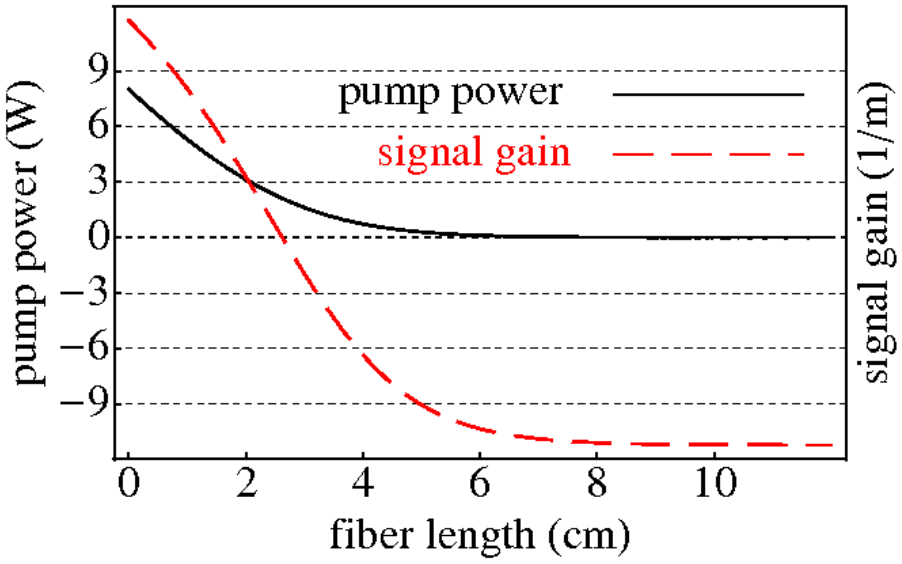

Fig. (4-1). Pump power and local signal gain are plotted as a function of the length of the GG-IAG fiber with 2% Yb^{+3} doping, where the core and cladding diameters are 200 and 340 μm, respectively. The signal is attenuated beyond the 27 mm length.

Another important consequence of the threshold gain in GG-IAG fibers is that Eqs. (4-1) and (4-2), indirectly, put a limit on the minimum value of the core radius of the fiber to support $LP_{01}$and LP_{11}, respectively. Below the threshold radius, the GG-IAG operation of the corresponding mode is not possible. In order to see this, consider an Nd^{+3}-doped fiber amplifier, where $g_{Nd} - g_{th}^{01} > 0$ must be satisfied for proper amplification of the LP_{01} mode, where g_{Nd} is the gain provided by the Nd^{+3}-doped core. However, $g_{Nd} < g_{max}$, where $g_{max} = \sigma^{(s)} N_{tot}$ is the maximum available signal gain in the limit of infinite pump power and zero signal power, and $\sigma^{(s)}$ is the emission cross section at the signal wavelength. This results in an absolute minimum in the desired radius of the core, as presented in Eqs. (4-3). Similarly, in (4-4), we present a minimum threshold radius for the excitation of the LP_{11}mode:

$$\min(a)_{01} = \left(\sqrt{\frac{133.8}{2n_0^3(-\Delta n)}}\frac{\lambda^2}{4\pi^2 g_{max}}\right)^{1/3} \tag{4-3}$$

$$\min(a)_{11} = \left(\sqrt{\frac{862.2}{2n_0^3(-\Delta n)}}\frac{\lambda^2}{4\pi^2 g_{max}}\right)^{1/3} \tag{4-4}$$

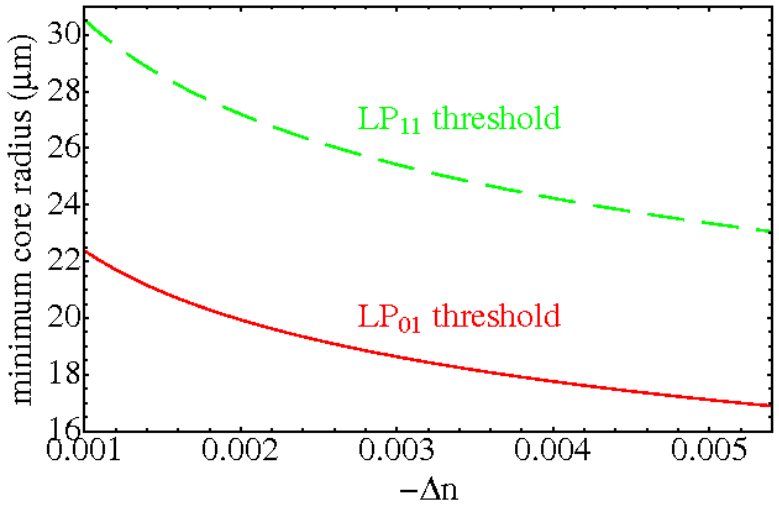

Fig. (4.2). Range of the core radius for operating in a single-mode regime in a 1% Nd dopant concentration versus different values of refractive index difference between the core and cladding, Δn, in the limit of infinite pump power and zero signal power.

In Fig. (4-2), we plot the minimum core radius for the case of 1% Nd^{+3} doping in the core, similar to the case studied by Sudesh et al. [5]. The values reported in Fig. (4-2) are merely lower bounds for the required value of radii and in practice, where the actual pump power is finite, g_{max} must be replaced with the actual calculated gain, thus resulting in larger required minimum radii. For example, for 10 W of pump power, which is far below that needed to obtain the saturated gain value of $\sigma^{(s)}N_{tot}$, we used the actual calculated value of the signal gain and found that the threshold radii for the excitation of the and modes are 37 and 51 μm, respectively. It must be noted that the core radius in [5] is 100 μm and the authors do not observe an LP_{11} excitation. Since we previously calculated the pump absorption at most at 3 dB level in this case and the pump power must be larger or equal to 10 W at any location along the fiber for an input power of 20 W, the only feasible explanations for the absence of LP_{11} mode can be either due to the lack of proper pump coupling, or excessive signal loss along the fiber. We note that in the presence of additional loss in the fiber, the threshold value for the radius is further raised, since the effective g_{max} is reduced. Typically, LP_{11} mode experiences more waveguide loss compared with LP_{01} mode; therefore, the threshold radius for the LP_{11} mode is raised substantially more due to the loss compared with the LP_{01} mode.

4.3 Improved Design Using a Tapered Cladding

Looking back at our arguments so far, one can correctly get a feeling that proper pump distribution is the key ingredient in designing GG-IAG fiber lasers and amplifiers, just as is the case in the conventional IG fibers. It must be noted that in conventional IG fibers, it is merely sufficient to create a population inversion to sustain a propagating mode without attenuation. However, in GG-IAG fibers, extra pump power is required to

establish a higher value of gain beyond the threshold value g_{th}^{01} to overcome the attenuation. In Fig. (4-1), we observed that the rapid pump absorption in the first few centimeters of the fiber deprived the rest of the fiber from the necessary pump power to maintain sufficient gain for the signal. In such situations, it is wise to design structures where the pump absorption efficiency is reduced in the beginning of the fiber, so that the pump power and consequently local signal gain can be distributed more evenly along the fiber. One method to achieve this for the end-pumped amplifier geometries is to taper the cladding cross section, while keeping the core size uniform, along the fiber. The optimal design of the fiber amplifier cladding area depends on whether the pump power is fully reflected at the end of the fiber or not. One expects higher values of signal gain, if the pump power is recycled by reflecting it back into the fiber.

In order to derive the appropriate equations, we make a few simplifying assumptions. Here, we assume that the pump power remains uniformly distributed across the fiber cross section; therefore, the pump power absorption efficiency scales with the pump overlap with the core as $\eta_p = \frac{A_{co}}{A_{cl}}$, where A_{co} is the area of the doped core and A_{cl} is the total area of the fiber cross section (core and cladding). Here, we note that A_{co} is fixed, while A_{cl} can vary along the fiber. In the following, we derive the appropriate equations to simulate the propagation of the pump and also the optimum form of the cladding radius as a function of the fiber length, in order to keep the pump intensity constant along the fiber. We note that in our derivation, the total amplifier gain is calculated in the small-signal limit [14]:

$$\frac{dP_p^+}{dz} = \eta_p\left(\sigma_{21}^p n_2 - \sigma_{12}^p n_1\right) N_{tot} P_p^+ \tag{4-5}$$

$$\frac{dP_p^-}{dz} = -\eta_p\left(\sigma_{21}^p n_2 - \sigma_{12}^p n_1\right)N_{tot}P_p^- \tag{4-6}$$

where the total pump intensity at each point along the fiber is given by

$$I_p(z) = \frac{P_p^+(z)+P_p^-(z)}{A_{cl}(z)} \tag{4-7}$$

n_1 and n_2 are the normalized ground-state and excited-state atomic-level populations, respectively, which participate in the lasing action, where $n_1 + n_2 = 1$. σ_{12}^p and σ_{12}^p are the absorption and emission cross sections at the pump wavelength. If we assume that the pump intensity is invariant along the fiber, i.e., $\frac{dI_p(z)}{dz} = 0$ ($I_p(z) = I_p(0)$), we can eliminate $P_p^-(z)$ from the aforementioned equations and derive

$$\frac{dA_{cl}}{dz} = \left(2\frac{P_p^+}{A_{cl}I_p(0)} - 1\right)A_{co}(\sigma_{21}^p n_2 - \sigma_{12}^p n_1)N_{tot} \tag{4-8}$$

Eqs (4-5), (4-6), and (4-8) can be solved simultaneously to obtain the pump power, as well as the cladding area variation along the length of the fiber amplifier. The equations must be solved iteratively, since one does not know a priori the contribution of $P_p^-(z = 0)$ to $I_p(0)$. The boundary condition at $z = 0$ should be set at $P_p^+(z = 0) = P_{p0}^+$, where P_{p0}^+ is the total input power into the fiber. The boundary condition at $z = L$ is set to $P_p^-(L) = R_p P_p^+(L)$, where R_p is the reflectivity of the end tip of the fiber amplifier at the pump wavelength.

4.4 Results and Discussion

In order to compare the performance of different amplifier designs, we calculate the total gain at the signal wavelength. In particular, for different designs of the fibers, we will compare the performance of nontapered-cladding designs with those of the tapered-

cladding designs. For tapered cladding, we are interested in two special cases of and $R_p = 0$ and $R_p = 100\%$.

In Table (4-1), we present the relevant design parameters belonging to seven different cases of GG-IAG fiber amplifiers. Cases 1–4, which are presented in Figs. (4-3a) to (4-3d), relate to GG-IAG fiber amplifiers with 1% Nd^{+3}-doped cores. The total gain for the amplifiers designed based on the parameters of case 1 is plotted in Fig. (4-3a). The contour plot in Fig. (4-3a) (left) shows the total signal gain as a function of the length of the GG-IAG fiber amplifier (horizontal axis) and the total input pump power (vertical axis); the cladding diameter is fixed (nontapered) in Fig. (4-3a) (left). Fig. (4-3a) (middle) presents a similar setup for case 1; however, the cladding is tapered in this case with $R_p = 0$. Fig. (4-3a) (right) presents again a similar set up for case 1; however, the cladding is tapered in this case with $R_p = 100\%$. Figs. (4-3a) to (4-3d) (Cases 1, 2, 3, and 4 in Table (4-1), respectively) are implemented for identical parameters, except that their core and cladding radii are different, as given in Table (4-1). We note that the values of the cladding radii in Table (4-1) represent the initial values at the beginning of the tapered fibers($z = 0$).

Table (4-1): Parameter for different Figures

Case	a (μm)	b (μm)	Core doping	L (cm)
1	50	150	1% Nd^{+3}	20
2	50	200	1% Nd^{+3}	20
3	100	200	1% Nd^{+3}	20
4	100	150	1% Nd^{+3}	10
5	100	200	1% Yb^{+3}	10
6	100	200	2% Yb^{+3}	7
7	100	200	10% Nd^{+3}	2.5

The maximum fiber length explored in Fig. (4-3d) is only $10\,cm$; the reason is that the radius of the tapered cladding gets too close to the radius of the core for the design to be practical. From Table (4-1) and Figs. (4-3a)-(4-3d), it is clear that in all these cases, a tapered cladding provides better gain than a nontapered cladding fiber. The designs where the pump power at the output end is recycled by using $R_p = 100\%$ show better performance over the designs where the exit pump power is wasted $R_p = 0$. If we compare Figs. (4-3a) and (4-3b), where the cladding radius is $b = 150\,\mu m$ and $b = 200\,\mu m$, respectively, we can conclude that a smaller cladding to core ratio in a nontapered GG-IAG is beneficial. This is because of the larger pump intensity in the core of the GG-IAG fiber with a smaller cladding radius, given a specific input pump power, which leads to a higher gain when the intensity is well below saturation. This difference is slightly less pronounced in the tapered GG-IAG fibers with $R_p = 0$; however, for $R_p = 100\%$;, the performances of the two GG-IAG fibers are virtually identical. If we compare Fig. (4-3a) and (4-3d) or Figs. (4-3b) and (4-3c), we observe that a larger ratio

of the core radius to the cladding radius (at fixed cladding radius) helps in obtaining a larger value of the gain, where this improvement is also more pronounced for $R_p = 100\%$ in tapered GG-IAG fiber amplifiers. Note that g_{th} is reduced for the larger values of the core radius, which contributes to the higher efficiency of the design.

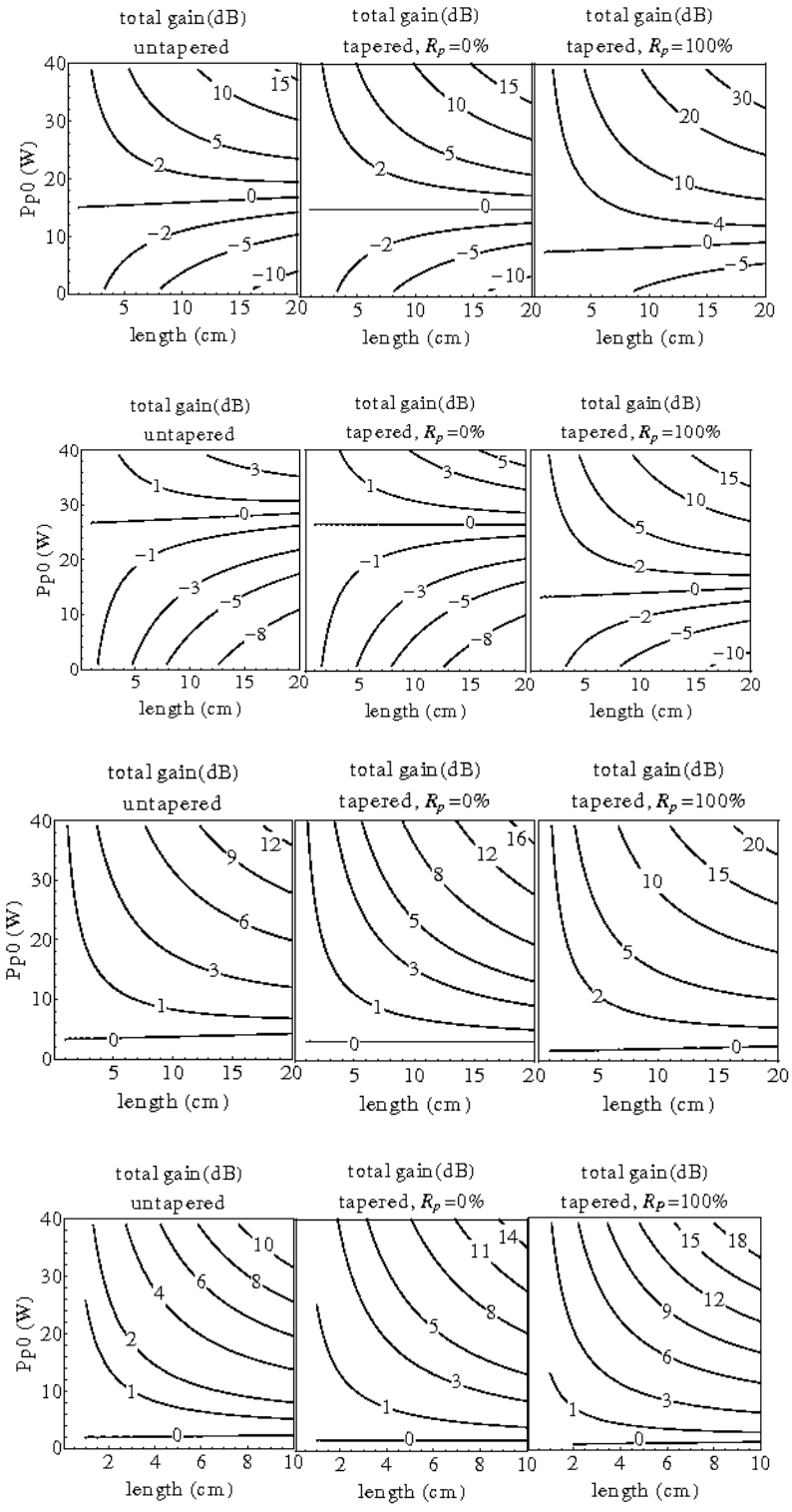

Fig. (4-3). Total gain of the amplifiers designed based on the parameters of Table (4-1) (1% Nd doped) are plotted in contour plots, as a function of the amplifier length and the input pump power. In each row, the left panel corresponds to the case of a nontapered cladding. The middle (right) panel corresponds to the case of a tapered cladding when $R_p = 0$ ($R_p = 100\%$) . The first, second, third, and fourth rows relate to Cases 1, 2, 3, and 4 in Table (4-1), respectively.

Next, we fix the core radius at $100\,\mu m$, and the initial value of the cladding radius $(z = 0)$ at $200\,\mu m$. We vary the doping material and doping concentration in the core and explore its impact on the performance of the GG-IAG fiber amplifier. In Fig. (4-4) (left), (middle), and (right), we compare the three cases of $1\%\,Yb^{+3}$ doping, $2\%\,Yb^{+3}$ doping, and $10\%\,Nd^{+3}$ doping, respectively. These correspond to Cases 5, 6, and 7 in Table (4-1), and are all implemented for a tapered cladding with $R_p = 100\%$. Fig. (4-4) (right) with $10\%\,Nd^{+3}$ doping (Case 7) should be compared with Fig. (4-3c) (right) with $1\%\,Nd^{+3}$doping (Case 3).While the maximum achievable gain is comparable between the two designs, the maximum gain for GG-IAG fiber amplifier with $10\%\,Nd^{+3}$doping (Case 7) is obtained over only $2.5\,cm$. From a practical point of view, the GG-IAG fiber amplifier with $1\%\,Nd^{+3}$ doping and $20\,cm$ length (Case 3) might be a much better design due to heat management issues.

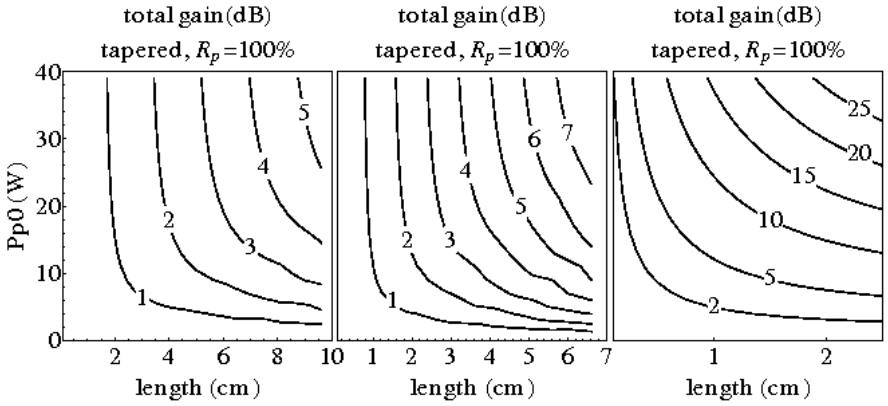

Fig. (4-4). Total gain of the amplifiers designed based on the parameters of Table (4-1) are plotted in contour plots, as a function of the amplifier length and the input pump power. In the left, middle, and right panels, we compare the three cases of $1\%\,Yb$, 2%Yb , and $10\%\,Nd$ doping, respectively. They all correspond to the case of a tapered cladding when $R_p = 100\%$, core radius of $100\,\mu m$, and the initial value of the cladding radius (z=0) of $200\,\mu m$. The left, middle, and right panels relate to Cases 5, 6, and 7 in Table (4-1), respectively.

As we already pointed out, one of the key issues in designing GG-IAG fiber amplifiers is to ensure that the pump power is not too quickly depleted along the fiber. Therefore, Nd^{+3}–doped amplifiers seem to generally perform better than Yb^{+3}–doped amplifiers, because Yb^{+3} atoms have a substantially larger pump absorption cross section and deplete the pump power too quickly, leading to the issues already elaborated in the discussions leading to Fig. (4-1). The lack of good performance in Yb^{+3}-doped GG-IAG fiber amplifiers is apparent when comparing Fig. (4-4) (left) and (middle) with (right) (Cases 5 and 6 with 7).

4.5 Practical Viability and Limitations

Cladding tapers (without tapering the core) can be achieved by etching the cladding using controlled hydrofluoric acid exposure with varying duration along the fiber [15]. For most practical applications, a moderate amount of tapering is sufficient to result in an improvement in the amplifier gain. In Fig. (4-5), we show the desired cladding radius for several different designs, all belonging to Case 3 in Table (4-1), related to Fig. (4-5), where the doping is 1% Nd^{+3} , the core radius is $a = 100\mu m$, and the initial value of the cladding radius at $z = 0$ is $b = 200\ \mu m$.

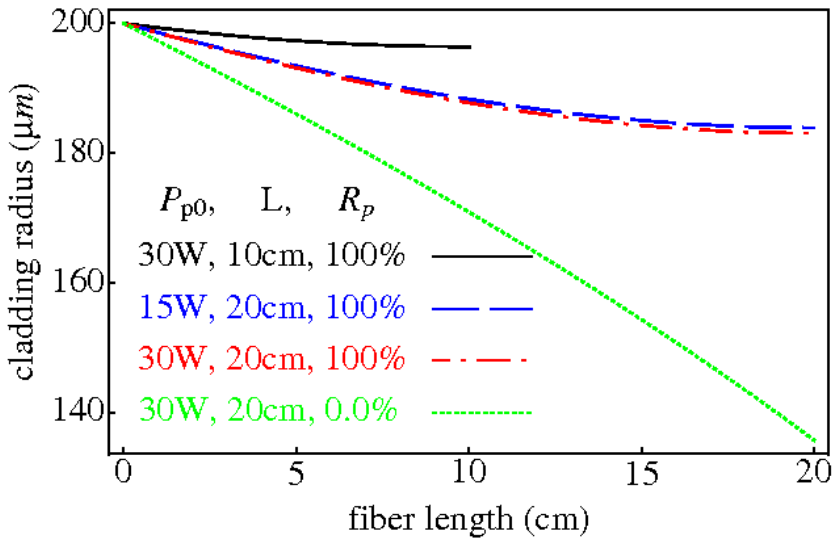

Fig. (4-5). Plots show the required tapered cladding radius as a function of the length for various designs corresponding to Case 3 in Table (4-1). Considerable tapering is required when no end mirror is used to recycle the pump power, i.e.,$R_p = 0\%$. The core radius for all cases is 100 μm.

In Fig. (4-5), the solid (black) line shows the desired tapered cladding radius for an $L = 10\ cm$ amplifier pumped with $P_{p0} = 30\ W$, with $R_p = 100\%$; we did not plot the line for the case of $P_{p0} = 15\ W$, because it was almost identical to the line for $P_{p0} = 30\ W$. The long-dashed (blue) line shows the required tapered cladding radius for an $L = 20\ cm$ amplifier pumped with $P_{p0} = 15\ W$, with $R_p = 100\%$; it can be compared with the required tapering radius in dot-dashed (red) line for twice the initial pump power, i.e., $P_{p0} = 30\ W$, where the two tapering designs are almost identical. We note that the exact value of the pump power does not have a significant impact on the ideal design of the taper, which is quite important in making the tapered design practical. We observe that in the aforementioned cases, the desired change in the cladding radius due to tapering is less than 10% of the cladding radius; however, the desired change is substantially larger when no end mirror is used to recycle the pump power, i.e., $R_p = 0\%$.

The dotted (green) line shows the desired tapered cladding radius for an $L = 20\ cm$ amplifier pumped with $P_{p0} = 30\ W$, with $R_p = 0\%$; the cladding radius must be tapered down to approximately $b = 135\ \mu m$ in this case, which is substantial and perhaps challenging in fabrication. Similarly, the required tapered cladding radius for an $L = 20cm$ amplifier pumped with $P_{p0} = 15\ W$, with $R_p = 0\%$ is almost identical to that of an identical case with $P_{p0} = 30\ W$ and its graph falls on the dotted (green) line. We note that in either case ($R_p = 100\%$ or $R_p = 0\%$), we would expect a less gentle tapering profile, if the pump power depletes too rapidly either due to a high dopant concentration or low pump power.

A limitation of the optimum designs presented in Figs. (4-3) and (4-4) may be that each optimum taper is tied to a particular choice of the fiber length and pump power, and is solved for by using (4-5), (4-6), and (4-8). In Fig. (4-6), we capture the impact of the deviations from the optimum design, both in the pump power and the taper profile, on the performance of the amplifier.

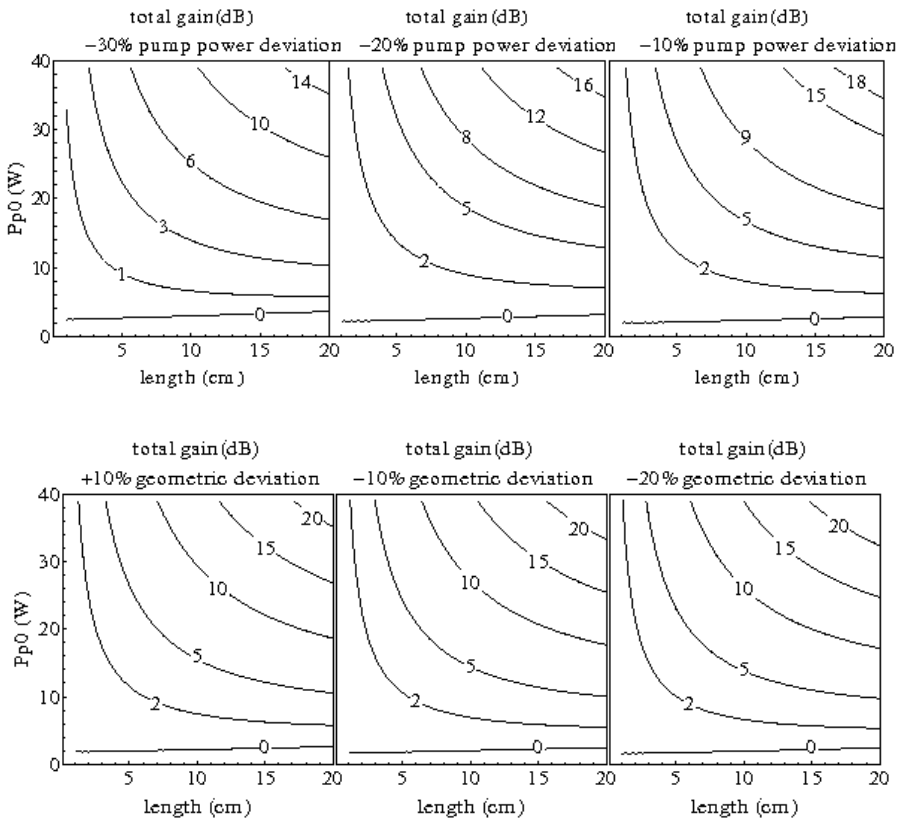

Fig. (4-6). Results presented in these subfigures are all related to Case 3 in Table (4-1) and should be compared with Fig. (4-3c)(right). (a) Left, middle, and right subfigures show the total value of amplifier gain, when the in-coupled pump power is reduced by 30%, 20%, and 10%, respectively, compared with the ideal case where all the pump power is coupled into the fiber amplifier. (b) Left, middle, and right subfigures show the total value of amplifier gain, when the tapering profile is modified from its optimum value by $\gamma = +10\%$, $\gamma = -10\%$, and $\gamma = -20\%$, respectively.

In Fig. (4-6a), we have chosen again Case 3 in Table (4-1), corresponding to Fig. (4-3c) (right) with $R_p = 100\%$ for our analysis. In each of the subfigures in Fig. (4-6a), used as the vertical axis indicates the total available pump power. Fig. (4-6a) (left), (middle), and (right) shows the total value of amplifier gain when the in-coupled pump power is reduced by 30%, 20%, and 10%, respectively, compared with the ideal case where all the pump power is coupled into the fiber amplifier, i.e., Fig. (4-3c)(right). The total amplifier gain deteriorates when the in-coupled pump power is reduced compared with the total available pump power for which the amplifier taper is optimized. We recall from Fig. (4-5) that variations around the exact value of the pump power do not have a

considerable impact on the desired tapering profile; therefore, the decrease in the total amplifier gain must be mainly attributed to the drop in the total available pump power, and not the incorrect tapering geometry.

In Fig. (4-6b), we explore the impact of the geometrical deviations from an ideal taper on the total amplifier gain. In each case, for each value of the input pump power $P_{p0}$and amplifier length L, we optimize the geometry as prescribed by (4-5), (4-6) and (4-8). We then multiply the cladding area profile by the factor $\eta(z) = (1 + \gamma z/L)$ to account for the imperfection in the tapering rate of the fiber; therefore, the actual taper area is in the form of $A_{cl}^{def}(z) = \eta(z)A_{cl}(z)$, instead of the originally optimized $A_{cl}(z)$. We then calculate the total amplifier gain using the same P_{p0} and L, yet using the updated $A_{cl}^{def}(z)$. Fig. (4-6b)(left), (middle), and (right) are for $\gamma = +10\%$, $\gamma = -10\%$, and $\gamma = -20\%$, respectively. We note that we assume no deviations at the input port of the fiber, i.e., $\eta(0) = 1$. We remind the reader that the aforementioned results are all for Case 3 in Table (4-1) and should be compared with Fig. (4-3) (right). In order to properly interpret the results in Fig. (4-6b), we need to remind the reader that the observed increase in the amplifier gain in Fig. (4-3c)(middle) compared with Fig. (4-3c)(left) is due to the higher pump intensity at each point along the fiber (except at z=0) in the tapered design, compared with the untapered. We referred to the tapered geometry obtained from solving (4-5), (4-6), and (4-8) as "optimum," because it would allow a uniform distribution of the pump power along the length of the fiber amplifier; however, this does not mean that we cannot obtain a higher amplifier gain if we deviate from the tapered geometry. This is especially true if the fiber amplifier works far below the saturation regime, where any decrease in the cladding radius can increase the total value

of the gain. This effect is no different from a "trivial" increase in the amplifier gain (per unit length) if the cladding radius is decreased even at z=0, as can be easily observed, e.g., by comparing Figs. (4-3a) and (4-3b). Unless additional constraints such as the minimum acceptable cladding radius are imposed on the design, neither our "optimum" tapered geometry, nor any other similar method can be used to maximize the amplifier gain; the "optimum" tapered geometry merely guarantees that the length of the amplifier is uniformly utilized and the heat is evenly generated along the fiber.

We are now ready to interpret the results in Fig. (4-6b) based on the above discussion. In Fig. (4-6b)(left) where $\gamma = +10\%$, the tapered cladding radius is larger at each point along the fiber compared to Fig. (4-3c)(right); therefore, the total amplifier gain is lower. In Fig. (4-6b)(middle) and (right) where $\gamma = +10\%$, $\gamma = -10\%$, and $\gamma = -20\%$,, respectively, the amplifier gain is comparable, though slightly higher, because the tapered cladding radius is smaller at each point along the fiber compared to Fig. (4-3c)(right). The fact that the gain obtained from the "optimum" tapered geometry is generally comparable to the gain obtained from the designs with $\gamma < 0$ (observed in other simulations not shown here, as well) indicates that the optimum tapered geometry is both a viable and robust design for such amplifiers.

Another important issue in the validity of (4-5), (4-6), and (4-8) is the assumption that the pump power is uniformly distributed across the fiber cross section. While common techniques such as the D-shaped cladding, or the proposed tapered cladding profile, can assist in uniformly distributing the pump power over the cladding area, the pump absorption rate in the core, as well as the transverse spatial coherence of the pump can play an important role in the distribution of the pump power. In general, lower values in

the transverse spatial coherence of the pump in overfilled pumping schemes can assist in redistributing the pump power, as the pump propagates and is absorbed in the core. We note the opposite case of a spatially coherent excitation, where it is even "theoretically" possible to excite only cladding modes with negligible overlap with the doped core, which can propagate unchanged along a uniform fiber. In practice, laser pumps are generally highly multimode, and the relative phases of these modes are random, resulting in a pump power profile with low spatial coherence. While detailed investigation of these issues is beyond the scope of this paper, we present two examples in a one-dimensional (1-D) slab waveguide and two-dimensional (2-D) fiber geometry that can quantify the validity of some of our assumption.

In Fig. (4-7) and (4-8), we explore two representative scenarios on pump absorption in $1-D$ and $2-D$ waveguides. The $1-D$ geometry is chosen to reduce the computational effort and simplify the modeling of the transverse spatial coherence of the input pump source. In Fig. (4-7), we plot the pump absorption in a $1-D$ slab waveguide. The total width of the slab waveguide (core and cladding) is $32\ \mu m$ with air jacket, and the width of the doped core is $20\ \mu m$. The refractive index of the cladding is 1.5, and the refractive index of the core is assumed to be $1.5-\Delta n$. The pump is assumed to be highly multimode ($\lambda = 808\ nm$) with a super-Gaussian profile overfilling the core and cladding area, with a transverse spatial coherence length of $4\ \mu m$.

We modeled the propagation of the pump and its absorption along the fiber using an in-house developed finite-difference beam-propagation-method (FD-BPM) code. The FD-BPM code is depicted in Appendix B. We considered two scenarios: one with labeled as undepressed index core in Fig. (4-7), and another with $\Delta n = 0.0045 + 0.0001i$ labeled

as depressed-index core. For each scenario, we launched 100 statistically independent pump profiles, all with the same spatial coherence length of 4 μm, and plotted the relative pump power as a function of propagation distance in Fig. (4-7). The error bars in each case signify one standard deviation around the mean value of the relative pump power averaged over the 100 independent simulations. For the simplified case of a uniformly distributed pump labeled as the "analytical model" in Fig. (4-7), we plot the relative pump power as $\frac{P(z)}{P_{po}} = \exp(-2\eta\Delta n_{im} k_0 z)$, where $k_0 = \frac{2\pi}{\lambda}$, z is the propagation distance, $\Delta n_{im} = 0.0001$ is the imaginary part of the refractive of the core, and $\eta = 20\,\mu m/32\,\mu m$ is the ratio of the core width to the cladding width; the analytical result is plotted as a solid (green) line in Fig. (4-7).

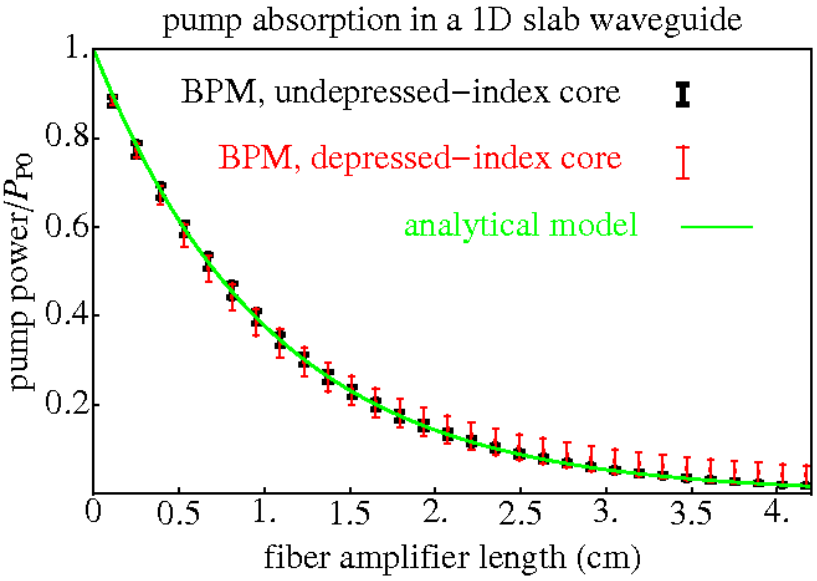

Fig. (4-7). Pump power relative to the initial value is plotted as a function of the propagation distance in a 1-D slab waveguide. The depressed-index core (GG-IAG), undepressed-index core (GG), and the analytical model based on the assumption of a uniform distribution of the pump power result in similar pump absorption profile.

Fig. (4-7) shows that the analytical model provides a reasonable estimate of the pump power along the fiber, which validates the assumptions used in this paper. Moreover, it is

clear that the pump absorption in a depressed-index core waveguide provides a greater sample-to-sample variability, but provides a very similar pump absorption profile to those of the undepressed-index core, and the analytical model. Therefore, the depressed-index core (the IAG nature of the waveguide) cannot be blamed for the lack of performance observed in GG-IAG fiber amplifiers and laser, as we discussed before.

Fig. (4-8) shows the pump absorption in a GG-IAG fiber. In order to make the computation less intensive, we set the core radius at $a = 10\,\mu m$ and the cladding radius at $b = 20\,\mu m$. The wavelength is $\lambda = 808\,nm$ and the step index is $\Delta n = 0.001$. The pump profile is chosen as a combination of the five lowest order Laguerre–Gauss functions with the fundamental radius at $8.5\,\mu m$. The power is equally distributed among modes but the relative modal phase is chosen randomly, with different sets for each of the 25 independent simulations used in this case. For each step in the z-direction for the $FD-BPM$ simulation, the laser-level population equations are solved point by point across the fiber, from which the local value of the gain and the local value of the imaginary part of the dielectric permittivity are calculated for the next z-step. The initial pump power is $P_{p0} = 0.1W$, which is physically equivalent to $P_{p0} = 10W$ in fiber geometries with $b = 20\,\mu m$. The core is assumed to be doped with $10\%\,Nd^{+3}$. The average pump power and its standard deviation are shown in Fig. (4-8) as discrete (red) dots with error bars and are compared with the semianalytical model in solid (green) line. The semi-analytical model assumes a uniform distribution of the pump power across the fiber at each step along the z-direction. The $FD-BPM$ model and the semi-analytical model show reasonable agreement; however, better agreement may be obtained when less spatially coherent pump is used.

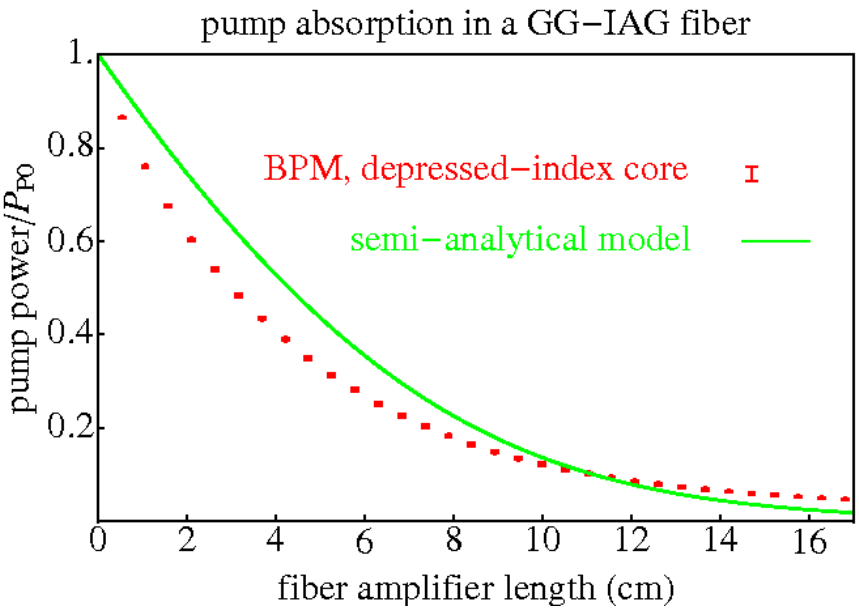

Fig. (4-8). Pump power relative to the initial value is plotted as a function of the propagation distance in a GG-IAG fiber, where the $FD-BPM$ propagation model is marked as the BPM depressed-index core (GG-IAG), and compares reasonably well with the semi analytical model based on the uniform distribution of the pump across the fiber. The core is assumed to be doped with 10% Nd^{+3}.

In the above discussions and the results presented in Figs. (4-7) and (4-8), we have shown sample models to justify our approximations in this paper. However, proper modeling of the pump propagation and making definitive arguments in justifying approximations will require accurate measurement of the pump coherence properties, and may be employed in optimizing the amplifier designs on a case-by-case basis. The difficulties in obtaining a desirable performance in such GG-IAG amplifiers will likely limit them to highly specialized applications where the large effective beam area and low nonlinearity are the primary design factors.

4.6 References

[1] A. E. Siegman, “Propagating modes in gain-guided optical fibers,” J. Opt. Soc. Amer. A, vol. 20, pp. 1617–1628, 2003.

[2] A. E. Siegman, “Gain-guided, index-antiguided fiber lasers,” J. Opt. Soc. Amer. A, vol. 24, pp. 1677–1682, 2007.

[3] A. E. Siegman, Y. Chen, V. Sudesh, M.-C. Richardson, M. Bass, P. Foy, W. Hawkins, and J. Ballato, “Confined propagation and near single mode laser oscillation in a gain guided, index antiguided optical fiber,” Appl. Phys. Lett., vol. 89, p. 251101, 2006.

[4] Y. Chen, T. McComb, V. Sudesh, M.-C. Richardson, and M. Bass, “Very large-core, single-mode, gain-guided, index-antiguided fiber lasers,” Opt. Lett., vol. 32, pp. 2505–2507, 2007.

[5] V. Sudesh, T. McComb, Y. Chen, M. Bass, M. Richardson, J. Ballato, and A. E. Siegman, “Diode-pumped 200 m diameter core, gainguided, index-antiguided single mode fiber laser,” Appl. Phys. B, vol. 90, pp. 369–372, 2008.

[6] W. Hageman, Y. Chen, X.Wang, L. Gao, G. U. Kim, M. Richardson, and M. Bass, “Scalable side-pumped, gain-guided index-anti-guided fiber laser,” J. Opt. Soc. Amer. B, vol. 27, pp. 2451–2459, 2010.

[7] X. Wang, Y. Chen, W. Hageman, G. U. Kim, M. Richardson, C. Xiong, J. Ballato, and M. Bass, “Transverse mode competition in gain-guided index antiguided fiber lasers,” J. Opt. Soc. Amer. B, vol. 29, pp. 191–196, 2012.

[8] K. M. Gundu, P. G. Yarandi, and A. Mafi, “Beam-quality factor of single-mode gain-guided fiber lasers,” Opt. Lett., vol. 35, pp. 4124–4126, 2010.

[9] P. G. Yarandi, K. M. Gundu, and A. Mafi, “On the beam profile and beam quality of gain-guided index-antiguided fibers with finite cladding boundary,” J. Opt. Soc. Amer. B, vol. 28, pp. 2430–2435, 2011.

[10] T. H. Her, “Gain-guiding in transverse grating waveguides for large modal area laser amplifiers,” Opt. Express, vol. 16, pp. 7197–7202, 2008.

[11] K. L. Yan, E. Y. Zhou, W. Wei, and B. Peng, “Efficiency of pump absorption in gain-guided and index-antiguided (GG-IAG) fiber,” J. Mod. Opt., vol. 57, pp. 480–484, 2010.

[12] M. Lu, W. Li,K. Zou, S.Dai,W.Wei, and B. Peng, “Yb doped 200 m diameter core, gain-guided index-antiguided fiber,” Appl. Phys. B, vol. 98, pp. 301–304, 2010.

[13] W. Li, M. Lu, Z. Yang, H. Guo, P. Wang, and B. Peng, “Fabrication and characterization of Yb doped gain-guided index-antiguided fiber with D-shaped inner cladding,” J. Opt. Soc. Amer. B, vol. 28, pp. 1498–1501, 2011.

[14] R. Paschotta et al., “Ytterbium doped fiber amplifiers,” IEEE J. Quantum Electron, vol. 33, no. 7, pp. 1049–1056, Jul. 1997.

[15] H. S. Haddock, P. M. Shankar, and R. Mutharasan, “Fabrication of biconical tapered optical fibers using hydrofluoric acid,” Mat. Sci. Eng.: B, vol. 97, pp. 87–93, 2002.

Chapter 5

Conclusion and Future Work

5.1 Conclusion

In this dissertation, we explore two issues that are of great importance to GG-IAG optical fiber lasers and amplifiers. The first problem is the large measured value of beam quality factor. This issue is raised because experimental works shows a single-mode profile but results in a large measured value of M^2. The second problem is the measured value of output power. It is too low. This question is important because GG-IAG fibers have the necessary ingredient, i.e., the large core size to lower nonlinearity for high power operation as fiber lasers and amplifiers. Therefore, investigation of these topics is necessary. It this thesis we find the answer for these two problems and the results are depicted in Chapters 2, 3 and 4.

In Chapter 2, we study the beam quality factor of GG-IAG fibers with infinite cladding size. We show that M^2 can be substantially larger than unity even for single-mode fibers in the $\mathrm{GG-IAG}$ region. The large value of M^2 in the $\mathrm{GG-IAG}$ region is the result of the long tail of the beam extending all the way into the cladding region, the truncation of which can lower M^2 substantially. The reported values of M^2 in several experiments on $\mathrm{GG-IAG}$ fiber lasers are in the range of $1.05-2.0$ [1–4]. For example, [1] reports $M^2 \leq 2$ for a $\mathrm{GG-IAG}$ optical fiber with a $100\,\mu m$ core diameter and a $250\,\mu m$ cladding diameter. Similarly, [2] reports $1.2 \leq M^2 \leq 1.5$, where the core and cladding diameters are $200\,\mu m$ and $340\,\mu m$, respectively. The cladding diameter is not much larger than the core diameter in either experiment. Consequently, the long cladding tail of the LP_{01} beam is truncated at the cladding-jacket interface over a large portion of the $\Delta N - G$ parameter space in the $\mathrm{GG-IAG}$ region. Therefore, it is not surprising that these experiments measure such low values of M^2.

In Chapter 2, we show that M^2 can be substantially larger than unity even for single-mode fibers in the GG-IAG region. We argue that the truncation of the beam profile due to an finite cladding diameter is responsible for the lower M^2 values observed in several experimental measurements. Therefore, in chapter 2, we introduce a Gaussian apodization to softly truncate the long intensity tail of the beam and explore its impact on M^2 values. In Chapter 3, for the first time to our knowledge, we present a rigorous analysis of the beam profile and M^2 for $\mathrm{GG-IAG}$ fibers with finite cladding diameters. Our analytical derivations presented in Appendix A are generally applicable to any step index optical fiber with an finite cladding diameter and gain in the core, such as the conventional double-cladding fiber lasers.

The reported values of M^2 in several experiments on GG-IAG fiber lasers are in the range of $1.05-2.0$ [1-6]. For example, [1] reports $M^2 \leq 2$ for a GG-IAG optical fiber with a 100 μm core diameter and a 250 μm cladding diameter ($\eta = 2.5$). Similarly, [5] reports $1.2 \leq M^2 \leq 1.5$, where the core and cladding diameters are 200 and 340 μm, respectively, where $\eta = 1.7$. These measurements are quantitatively consistent with our results presented in Fig. (3-4) for $\Delta N \leq -1000$. Reference [6] reports $M^2 \approx 1.4$ for a GG-IAG optical fiber with a 100 μm core diameter and a 250 μm cladding diameter ($\eta = 2.5$). This value of M^2 is slightly lower than what we expect from our simulations. However, there are uncertainties associated with M^2 measurements as is clear from the difference between the reported results of [1,6]. Therefore, it is reasonable to expect some slight differences between theory and experiment.

GG-IAG fibers provide a rich parameter space to explore and design unconventional optical-fiber-based devices. We think that GG-IAG fiber lasers and amplifiers have great

potential in systems where the reduction of nonlinearity is critical, at the expense of efficiency. While low efficiency is somewhat inherent in their nature because of the presence of a gain threshold which can lead to considerable signal leakage, much can be gained with proper design and optimization of such systems. Conventional wisdom blames the poor efficiency of GG-IAG fiber amplifiers and lasers on the IAG nature of the core at the pump wavelength, which repels the pump into the cladding. However, we think that the lack of efficiency is chiefly due to the nature of such waveguides and must be addressed by proper design and perhaps unconventional techniques. In Chapter 4, we suggest that the tapering of the cladding in GG-IAG fibers significantly improves the total signal gain, since it can potentially remedy the improper pump distribution along the fiber. We also point out the substantial inherent signal power leakage into cladding, especially in lasers with high reflectivity mirrors, which can be either a safety concern or serve as a characterization and measurement opportunity. Finally, we would like to emphasize that much of our findings are related to the case of end pumping which we think is a more viable path to designing future $GG-IAG$ amplifiers in practical applications.

5.2 Future work

The present dissertation emphasized on solving the two important issues on GG-IAG fibers which were beam quality factor and low output power. The first and important future work is setting up an experiment to test the result of theoretical work we carry out on GG-IAG fiber in Chapter 4. We designed a tapered GG-IAG fiber. Our analysis shows that tapering improves the output power significantly.

The effect of thermal loading on output power of GG-IAG fibers, calculating the bending loss and studying the different cladding design for optimizing the pump absorption can also be investigated for future works.

5.3 Reference

[1] A. E. Siegman, Y. Chen, V. Sudesh, M. C. Richardson, M. Bass, P. Foy, W. Hawkins, and J. Ballato, "Confined propagation and near single mode laser oscillation in a gain guided, index antiguided optical fiber," Appl. Phys. Lett. 89, 251101 (2006).

[2] T. McComb, V. Sudesh, Y. Chen, M. Bass, M. C. Richardson, J. Ballato, and A. E. Siegman, "Single Mode Lasing in a 200m Diameter Core Gain-guided Index Anti-guided Diode End Pumped Fiber," in Lasers and Electro-Optics Society, 242-243 (2007).

[3] Y. Chen, V. Sudesh, T. McComb, M. C. Richardson, M. Bass, and J. Ballato, "Lasing in a gain-guided index antiguided fiber," J. Opt. Soc. Am. B 24, 1683 (2007).

[4] Y. Chen, T. McComb, V. Sudesh, M. C. Richardson, and M. Bass, "Very large-core, single-mode, gainguided, index-antiguided fiber lasers," Opt. Lett. 32, 2505 (2007).

[5] V. Sudesh, T. McComb, Y. Chen, M. Bass, M. Richardson, J. Ballato, and A. E. Siegman, "Diode-pumped 200 μm diameter core, gain-guided, index-antiguided single mode fiber laser," Appl. Phys. B 90, 369–372 (2008).

[6] W. Hageman, Y. Chen, X. Wang, L. Gao, G. U. Kim, M. Richardson, and M. Bass, "Scalable side-pumped, gain-guided index-anti- guided fiber laser," J. Opt. Soc. Am. A 27, 2451–2459 (2010).

Appendix A: Analytical formula for M^2 Calculation

In this appendix we present closed-form analytical expression for the parameters defined in Eqs. (3-22) and (3-23), which can be used to evaluate the M^2 parameter. First the following functions and functionals were introduced.

$$\zeta_{m,n,\tilde{u}}^{p,q} = (p\tilde{u}^2 + q\tilde{u}^{*2})^m/(p\tilde{u}^2 - q\tilde{u}^{*2})^n, \tag{B1}$$

$$F_n(x,X,Y) = x^* X_n(x) Y_n'(x^*) - x X_n'(x) Y_n(x^*), \tag{B2}$$

$$G_n(x,X,Y) = X_n(x) Y_n(x^*)\ , \tag{B3}$$

$$P_n(M,\tilde{u},\tilde{a},X,Y,p,q) = M\tilde{a}^2 \zeta_{0,1;\tilde{u}}^{p,q}\, F_n(\tilde{u},X,Y)\ , \tag{B4}$$

$$Q_n(M,\tilde{u},\tilde{a},X,Y,p,q) = 2M\tilde{a}^4 \zeta_{1,2;\tilde{u}}^{p,q}\, G_n(\tilde{u},X,Y) + 4M|\tilde{u}|^2 \tilde{a}^4 \zeta_{0,2;\tilde{u}}^{p,q}\, G_{n+1}(\tilde{u},X,Y) +$$

$$\tilde{a}^2(1 - \zeta_{1,2;\tilde{u}}^{p,q})\, P_n(M,\tilde{u},\tilde{a},X,Y,p,q), \tag{B5}$$

$$R_n(M,\tilde{u},\tilde{a},X,Y,p,q) = M\tilde{a}^2 F_n(\tilde{u},X,Y) - \tilde{a}^{-2} \zeta_{1,0;\tilde{u}}^{p,-q}\, Q_n(M,\tilde{u},\tilde{a},X,Y,p,q), \tag{B6}$$

$$U_n(M,\tilde{u},\tilde{a},X,Y,p,q) = \tilde{a}^{-2}|\tilde{u}|^2\, P_n\big(M,\tilde{k},\tilde{a},X,Y,p,q\big), \tag{B7}$$

$$S_n(I,M,\tilde{u},X,Y,p,q) = I_n(M,\tilde{u},b,X,Y,p,q) - I_n(M,\tilde{u},a,X,Y,p,q), \tag{B8}$$

$$T_n(I) =$$

$$I_n\left(\left|\tilde{A}\right|^2, u_1, a, J, J, 1, 1\right) - I_n\left(\left|\widetilde{D}\right|^2, u_3, b, K, K, -1, -1\right) + S_n\left(I, \left|\tilde{B}\right|^2, u_2, J, J, 1, 1\right) +$$

$$S_n\big(I, \tilde{B}\tilde{C}^*, u_2, J, K, 1, -1\big) + S_n\big(I, \tilde{C}\tilde{B}^*, u_2, K, J, -, +\big) + S_n(I, |\tilde{c}|^2, u_2, K, K, -, -), \tag{B9}$$

In the above expression p and q each can values of ± 1, which are shortened to $\pm$ in Eq. (A9). X_n and Y_n each represent one of the Bessel functions J_n and K_n, respectively. We also have

$$\tilde{A} = \frac{1}{J_0(u_1)}, \qquad \tilde{B} = \frac{1}{L_0(u_1)}\frac{S_2}{S_1}, \qquad \tilde{C} = \frac{1}{L_0(u_2)}, \qquad \widetilde{D} = \frac{L_0(u_2\eta)}{L_0(u_2)}\frac{1}{K_0(u_3)}, \tag{B10}$$

Equipped with these functions and functionals, we can obtain the following explicit expressions for the parameters of interest:

$$\frac{1}{\widetilde{N}^2} = 2\pi T_0(P), \tag{B11}$$

$$\sigma_x^2(z_0) = \pi\widetilde{N}^2 T_0(Q), \tag{B12}$$

$$A(z_0) = i\pi\widetilde{N}^2 T_0(R/2), \tag{B13}$$

$$B(z_0) = \pi\widetilde{N}^2 T_1(U), \tag{B14}$$

We note that the analytical derivations involve the evaluation of complex valued moments of products of Bessel functions, which are beyond the scope of the present research. The works demonstrate in Appendix A, had been done mainly by Dr. Krishna Mohan Gundu in our group, and we compared and confirmed his analytical results with our numerical calculation.

Appendix B: FD-BPM Code

```
close all;
clear all;
clc;
format long
%+++++++++++++++++++++++++++++++++++++++++++++++++++%
%                BPM-Code Laser Simulation   -10 w                %
%+++++++++++++++++++++++++++++++++++++++++++++++++++%
% tic
%===================================================%
%                              coefficient                              %
%===================================================%
%-------------  Constant   -------------%
mu0=4*pi*10^-7;
eps0=8.85*10^-12;
%-------------  Refractive Index   -------------%
n_b=1.0;
n_core_real=1.459;
n_cladd=1.46;
n0=1.459;
%-------------  Structure   -------------%
x1 = -25;
```

```
x2 =25;
y1 = -25;
y2 =25;
num_samples = 90;
dx = (x2-x1)/num_samples;
dy = (y2-y1)/num_samples;
y_struc=y1;
radius_core=10;
radius_cladding=20;
%-------------  Distance   -------------%
lambda=0.976;
k0 = 2*pi/lambda;
dz =dx^2*k0*real(n0)/10;
z_step=600001; % 0.144957303710435
Distance=z_step*dz
%-------------  Runge kutta Method   -------------%
z0=0;
%                          Source                          %
So=zeros(num_samples,num_samples);
 for ii=1:num_samples
    xx(ii)=x1+(ii).*dx;
    for jj=1:num_samples
      yy(jj)=y1+(jj).*dy;
```

```
            if  xx(ii)^2+yy(jj)^2<=radius_cladding^2
                    phi=rand(1,1)  ;
          So(ii,jj)=1*10^4*exp(i*phi*2*pi);
       end
    end
    jj=jj+1;
 end
 source=So;
surf(xx,yy,abs(So) )
shading interp
%  view(0,90)
%  axis off
%  axis equal
title('Source')
%=======================================%
%                    Power of the Source                    %
%=======================================%
new_matrix=abs(So).^2;%./sqrt(mu0./eps0./epsilon);
jame1=sum(new_matrix(:,:)*dx*10^-6);
jame11=sum(jame1*dx*10^-6);
Power_source=jame11
%=====================================%
%                    new way                          %
```

```
%===================================%
for ii=1:num_samples
      xx(ii)=x1+(ii).*dx;
   for jj=1:num_samples
            yy(jj)=y1+(jj).*dy;
            if ( xx(ii)^2+yy(jj)^2 <= radius_cladding^2)
         So_new(ii,jj)=So(ii,jj);
      else
         So_new(ii,jj)=0;
      end
           end
      jj=1;
   end
new_matrix1=abs(So_new).^2;%./sqrt(mu0./eps0./epsilon);
jame1_new=sum(new_matrix1(:,:)*dx*10^-6);
jame11_new=sum(jame1_new*dx*10^-6);
Power_source_new=jame11_new
for l=1:z_step
 % waitbar(l/z_step)
%============================== ======%
%                    Definig structure                    %
%===================================%
%-------------  Epsilon   -------------%
```

```
epsilon=zeros(num_samples,num_samples);
for ii=1:num_samples
   x(ii)=x1+(ii).*dx;
      for jj=1:num_samples
      y(jj)=y1+(jj).*dy;
         epsilon(ii,jj)=n_b^2;
           if ((x(ii))^2+ (y(jj))^2)<=radius_cladding^2 && ((x(ii))^2+
(y(jj))^2)>=radius_core^2
  epsilon(ii,jj)=(n_cladd).^2;
      end
      if ((x(ii))^2+ (y(jj))^2)<=radius_core^2
      Intensity=abs(source(ii,jj))^2;
   epsilon(ii,jj)=(n_core_real-1i*ImaginaryR(Intensity,dz,lambda)).^2;
      end
      end
     jj=1;
end
%==================================%
%                    Field                          %
%==================================%
y=source;
k1=func2D(y,n0,k0,num_samples,dx,dy,dz,epsilon);
%--------------------------------------------------------------------%
```

```
z1=z0+dz/2;
y11=source+k1*dz/2;
y=y11;
k2=func2D(y,n0,k0,num_samples,dx,dy,dz,epsilon);
z1=z0+dz/2;
y11=source+k2*dz/2;
y=y11;
k3=func2D(y,n0,k0,num_samples,dx,dy,dz,epsilon);
z1=z0+dz;
y11=source+k3.*dz;
y=y11;
k4=func2D(y,n0,k0,num_samples,dx,dy,dz,epsilon);
Yout=source+dz/6*(k1+2*k2+2*k3+k4);
%=====================================%
%                  boundry condition                  %
%=====================================%
 for pp=1:num_samples
        if (Yout(pp,num_samples-2) ~= 0 )
       coef3=1i/dx*log(Yout(pp,num_samples-1)./Yout(pp,num_samples-2));
       if real(coef3)<0
          coef3=0;
       end
          Yout(pp,num_samples)=Yout(pp,num_samples-1)*  exp(-1i*dx* coef3);
```

```
    end
    if (Yout(num_samples-2,pp) ~= 0 )
        coef33=1i/dx*log(Yout(num_samples-1,pp)./Yout(num_samples-2,pp));
        if real(coef33)<0
            coef33=0;
        end
            Yout(num_samples,pp)=Yout(num_samples-1,pp)*  exp(-1i*dx*coef33);
    end
   if (Yout(pp,3) ~= 0)
      coef4=1i/dx*log(Yout(pp,2)  ./   Yout(pp,3));
      if real(coef4)<0
         coef4=0;
      end
         Yout(pp,1)=Yout(pp,2)*   exp(-1i*dx*coef4);
   end
   if (Yout(3,pp) ~= 0)
      coef44=1i/dx*log(Yout(2,pp)  ./   Yout(3,pp));
      if real(coef44)<0
         coef44=0;
      end
         Yout(1,pp)=Yout(2,pp) *  exp(-1i*dx* coef44);
   end
end
```

```
%====================================%
%                Save Field          %
%====================================%
if rem (l,1000) ==1
%   output_name = [ 'Output_field' , num2str(l) ];
%   yo=abs(Yout);
%   save(output_name,'yo','-ASCII');
%====================================%
%              Power of the output   %
%====================================%
for ii=1:num_samples
   xx(ii)=x1+(ii).*dx;
   for jj=1:num_samples
      yy(jj)=y1+(jj).*dy;
      if ( xx(ii)^2+yy(jj)^2 <= radius_cladding^2)
         So_new_out(ii,jj)=Yout(ii,jj);
      else
         So_new_out(ii,jj)=0;
      end
   end
   jj=1;
end
```

```
new_matrix1_out=abs(So_new_out).^2;%./sqrt(mu0./eps0./epsilon);
jame1_new_out=sum(new_matrix1_out(:,:)*dx*10^-6);
jame11_new_out=sum(jame1_new_out*dx*10^-6);
Power_out_new(l)=jame11_new_out;
%====================================%
%                Ratio Power                %
%====================================%
ratio(l)=Power_out_new(l)/Power_source_new;
z(l)=l*dz;
end
%====================================%
%                end of Code                %
%====================================%
source=Yout;
z0=z1;
end
% toc
% figure;
% contourf(epsilon)
% axis equal
% axis off
figure;
surf(xx,yy,abs(Yout))
```

```
shading interp

title('Output')

xlabel('X')

ylabel('Y')

zlabel('Amplitude')

figure;

plot(z,ratio)

grid on

xlabel('Z')

ylabel('Ratio of Power')

save ratio ratio -ascii ;

save Power_Output Power_out_new -ascii ;

save Power_source Power_source_new -ascii ;
```

```
function f = func2D(y,n0,k0,num_samples,dx,dy,dz ,epsilon)
 source1=y;
f_3=(-i*k0)/(2*n0)*(epsilon - n0^2).*source1;
% ------------------------------------------------------%
source_m=[source1 0.5*source1(:,num_samples)];
source_m(:,1)=[];
source_p=[0.5*source1(:,1) source1];
source_p(:,num_samples+1)=[];
f1=(source_m-2.0.*source1+source_p);
f_x=-i/(2*n0*k0).*f1./(dx.^2);
% ------------------------------------------------------%
source_m=[source1; 0.5*source1(num_samples,:)];
source_m(1,:)=[];
source_p=[0.5*source1(1,:); source1];
source_p(num_samples+1,:)=[];
f1=(source_m-2.0.*source1+source_p);
f_y=-i/(2*n0*k0).*f1./(dy.^2);
 f=f_x+f_y+f_3;
```

```
function f =ImaginaryR(Intensity,dz,lambda)
%=====================================%
%                    Calculating n1 -- n2                    %
%=====================================%
%-------------  Constant   -------------%
mu0=4*pi*10^-7;
eps0=8.85*10^-12;
%-------------  coefficient   -------------%
dz=dz*10^-6;
sigma12p = 1.5*10^-24;
simga21p = 3.5*10^-24;
sigma12s = 0.0005*10^-24;
simga21s = 0.6*10^-24;
wavelengthpump = lambda*10^-6;
wavelengthsignal = 1.036*10^-6;
h = 6.62*10^-34;
c=1/sqrt(mu0*eps0);
signalintensity0 = 0;
A21 = 1/(770*10^-6);
freqpump=c/wavelengthpump;
freqsignal=c/wavelengthsignal;
R120 = sigma12p*Intensity/h/freqpump;
w120 = sigma12s*signalintensity0/h/freqsignal;
```

```
R210 = simga21p*Intensity/h/freqpump;

w210 = simga21s*signalintensity0/h/freqsignal;

etap=1;%(radius_core/radius_cladding)^2;

ppm=10101.010101;

Ntot= ppm*6.022e+20/173.04*2648;

%=======================================%

%                calculating alpha - imaginary part              %

%=======================================%

n2 =(R120+w120)/(R120+w120+R210+w210+A21) ;

n1=1-n2;

alpha=-etap*(simga21p*n2 - sigma12p*n1)*Ntot;

alpha_dB= 4.343*alpha;

f=alpha*wavelengthpump/4/pi;
```

CURRICULUM VITAE

Parisa Gandomkar Yarandi

Doctoral Philosophy, Electrical Engineering, Minor: Mathematics
University of Wisconsin- Milwaukee, Milwaukee, WI, USA.
Dissertation Title: "Gain-Guided, Index Anti-Guided Fiber Laser and Amplifier"
Advisor: Dr. Arash Mafi

Technical Skills

- Optics and Photonics
- High Power Fiber Lasers and Amplifiers
- Fiber Optics/ Fiber Optic Communication.
- Photonic Crystal De-Multiplexer
- Modeling and simulation with FDTD
- Experimental work in the field of optics
- Birefringence in Photonic Crystal Fibers
- Nonlinear Fiber Optics
- Photonic Crystal Fibers
- Optical Telecommunications
- Bioelectromagnetics
- Electromagnetics
- Fiber Optic Sensors

Scientific Publications

1. P. Gandomkar Yarandi, S. Karbasi, and A. Mafi, "Improving the Power Efficiency in End-Pumped Gain-Guided Index-Antiguided Fiber Amplifiers", J. of Lightwave Technology, 30, 3203-3210, (2012).

2. S. Karbasi, C. R. Mirr, R. J. Fraizer, P. Gandomkar Yarandi, K. W. Koch, and A. Mafi, "Detailed investigation of the impact of the fiber design parameters on the transverse Anderson localization of light ", Optics Express, 20, 18692-18706, (2012).

3. S. Karbasi, C. Mirr, P. Gandomkar Yarandi, R. Frazier, K. Koch, and A. Mafi, "Observation of Transverse Anderson Localization in an Optical Fiber ", Optics Letters, 37, 2304-2306, (2012).

4. P. Gandomkar Yarandi, K. Mohan Gundu, and A. Mafi, "On the beam profile and beam quality of gain-guided index-antiguided fibers with finite cladding boundary", J. Opt. Soc. Am. B, 28, 2430-2435, (2011).

5. E. Forati, A. D. Mueller, P. Gandomkar Yarandi, and G. W. Hanson,"A New Formulation of Pocklington's Equation for Thin Wires Using the Exact Kernel", IEEE Trans. Antennas Propagation, 59, 4355-4360, (2011).

6. K. Mohan Gundu, P. Gandomkar Yarandi, and A. Mafi, "Beam-quality factor of single-mode gain-guided fiber lasers", Opt. Letters, 35, 4124-4126, (2010).

7. P. Gandomkar Yarandi, S. Karbasi and A. Mafi, "Power Efficiency in Cladding-Tapered Gain-Guided, Index-Antiguided Fiber Amplifiers", poster presentation in Frontiers in Optics (FiO), Rochester, (2012).

8. P. Gandomkar Yarandi and A. Mafi, "Poor Power Efficiency in Gain-Guided Index-Antiguided Fiber Amplifiers and Lasers", Oral presentation in CLEO, San Jose, (2012).

9. A. Mafi and P. Gandomkar Yarandi, "Ultra-large-core index-antiguiding gain-guiding fiber lasers for high power applications", AFOSR 11, Albuquerque, New Mexico, (2011).

10. P. Gandomkar Yarandi and A. Mafi, "Beam quality factor of gain-guided index-antiguided fiber laser with a finite cladding diameter", Oral presentation in Frontiers in Optics (FiO), San Jose, (2011).

11. P. Gandomkar Yarandi and A. Mafi, "Birefringence in Photonic Crystal Fibers: Cladding Lattice Shape versus Unit-Cell Anisotropy", Oral presentation in Frontiers in Optics (FiO), Rochester, (2010).